1   **Evaluation of aerosol optical depths and clear-sky radiative fluxes of the**

2   **CERES Edition 4.1 SYN1deg data product**

5   David W. Fillmore[1], David A. Rutan[2], Seiji Kato[3], Fred G. Rose[2],

6   and Thomas E. Caldwell[2]

8   [1]University Center for Atmospheric Research, Boulder, CO. 80307, USA

9   [2]SSAI, Hampton, VA, 23666, USA

10   [3]NASA Langley Research Center, Hampton, VA, 23666, USA

14   Submitted to

15   *Atmospheric Chemistry and Physics*

16   April 2021

20   ___________________

22   *Corresponding author address:* David W Fillmore,
23   University Center for Atmospheric Research
24   P.O. Box 3000
25   Boulder, CO 80307
26   E-mail: david.w.fillmore@ucar.edu

27 Abstract

28 Aerosol optical depths (AOD) used for the Edition 4.1 Clouds and the Earth's Radiant

29 Energy System (CERES) Synoptic (SYN1deg) are evaluated. AODs are derived from

30 Moderate Resolution Imaging Spectroradiometer (MODIS) observations and assimilated

31 by an aerosol transport model (MATCH). As a consequence, clear-sky AODs closely

32 match with those derived from MODIS instruments. AODs under all-sky conditions are

33 larger than AODs under clear-sky conditions, which is supported by ground-based

34 AERONET observations. When all-sky MATCH AODs are compared with Modern-Era

35 Retrospective Analysis for Research and Applications (MERRA2) AODs, MATCH

36 AODs are generally larger than MERRA2 AODS especially over convective regions (e.g.

37 Amazon, central Africa, and eastern Asia). The difference is largely due to the differing

38 methods of assimilating the MODIS AOD data product and the use of quality flags in our

39 assimilation. Including AODs with larger retrieval uncertainty makes AODs over the

40 convective regions larger. When AODs are used for clear-sky irradiance computations

41 and computed downward shortwave irradiances are compared with ground-based

42 observations, the computed instantaneous irradiances are 1% to 2% larger than observed

43 irradiances. The comparison of top-of-atmosphere clear-sky irradiances with those

44 derived from CERES observations suggests that AODs used for surface radiation

45 observation sites are larger by 0.01 to 0.03, which is within the uncertainty of

46 instantaneous MODIS AODs. However, the comparison with AERONET AOD suggests

47 AODs used for computations over desert sites are 0.08 larger. The cause of positive

48 biases of downward shortwave irradiance and positive bias in AOD for the desert sites is

49 possibly due to dust particle size and their distribution as defined by the MATCH

50 transport model and the transfer of that information into the radiative transfer model.

51 **1. Introduction**

52   Accurate estimates of the radiative effects of clouds and aerosols are essential for

53 an understanding the radiative forcing to the Earth's climate system (Bauer and Menon,

54 2012, Boucher et al. 2013). In addition, through the reflection and absorption of solar

55 radiation, and the absorption and emission of terrestrial thermal radiation, clouds and

56 aerosols affect the radiative heating of both the atmosphere and the surface, which in turn

57 governs the atmospheric circulation and the hydrological cycle (e.g. Stephens et al. 2020,

58 L'Ecuyer et al. 2015). Under the Earth Observing System (EOS) program, the National

59 Aeronautics and Space Administration (NASA) has placed into orbit a series of satellites

60 devoted to long term observations of the climate state. Among these are Terra and Aqua,

61 the flagship satellites of the EOS. Central to observation of climate evolution are

62 Moderate Resolution Imaging Spectroradiometer (MODIS) and the Clouds and the

63 Earth's Radiant Energy System (CERES) instrument pairs that fly on both the Terra

64 (March 2000 - present) and the Aqua (July 2002 - present) platforms (Wielicki et al.

65 1996). Additional CERES instruments were launched (October 2011) upon the Suomi

66 National Polar-orbiting Partnership (NPP) satellite along with the MODIS successor, the

67 Visible Infrared Imager Radiometer Suite (VIIRS), and on the NOAA-20 satellite

68 (November 2017). In addition to observations from these satellites, the CERES mission

69 also integrates observations from the Geostationary Operational Environmental Satellites

70 (GOES) (West and East), as well as other geostationary satellites around the globe, for

71 full diurnal coverage of clouds and radiation.

72   The CERES instruments measure broadband radiances over the solar spectrum

73   (shortwave), the thermal infrared (longwave radiance is obtained from a total channel

74   minus the shortwave channel), and the near infrared atmospheric window, with frequent

75   on-board calibration. CERES measurements, in conjunction with MODIS information,

76   are used to infer broadband irradiances through empirical angular distribution models

77   (ADMs). Geosynchronous satellite imagery observes the diurnal cycle of clouds, which is

78   not fully sampled by the polar orbiting satellites upon which CERES and MODIS reside.

79   While top-of-atmosphere (TOA) irradiances are derived from broadband

80   radiances measured by CERES instruments (Loeb et al. 2005; Su et al. 2015), surface and

81   in atmosphere irradiances are computed with a radiative transfer model. Inputs used for

82   the computations include cloud properties derived from MODIS and geostationary

83   satellites, aerosol optical depth derived from MODIS radiances, and surface albedo

84   derived from MODIS and CERES observations (Rutan et al. 2009). Temperature and

85   humidity profiles are provided by a reanalysis product produced by the NASA Goddard

86   Modeling and Assimilation Office (GMAO).

87   Irradiances at the surface produced by the CERES team have been compared with

88   surface observations (Rutan et al. 2015; Kato et al. 2013, 2018). These comparisons are

89   for all-sky conditions (i.e. including any clouds). Irradiances under clear-sky conditions

90   are not explicitly separated from all-sky conditions in the evaluations. There are several

91   reasons that impede efforts at rigorous validation of clear-sky irradiances with surface

92   observations; 1) a clear-sky condition at a given site does not persist over a long time

93   (e.g. a month or longer), 2) there are mismatches of clear-sky conditions determined by

94   satellite- and ground-based instruments, and 3) field-of-view size between CERES

95   instruments and ground-based radiometers differ.

96   Despite difficulties in evaluating computed clear-sky irradiances, they play an

97   important role in quantifying aerosol and cloud radiative effects (Loeb and Su 2010;

98   Soden and Chung 2017). Therefore, the uncertainty in surface irradiances need to be

99   understood in order to assess the uncertainty in aerosol and cloud radiative effect. This

100   work is the first attempt by the CERES team to evaluate clear-sky surface irradiances

101   provided by its data products. One of the essential variables in computing clear-sky

102   irradiances is aerosol optical depth. In this paper, we evaluate aerosol optical depth used

103   for irradiance computations in the CERES project and analyze how the error propagates

104   to clear-sky surface irradiances. Computations of surface irradiances provided by Edition

105   4.1 SYN1deg data products use aerosol optical depth derived by a chemical transport

106   model [The Model for Atmospheric Transport and Chemistry (MATCH, Collins et al.

107   2001)] that assimilates MODIS-derived aerosol optical depth. In Section 2, we explain in

108   the MATCH aerosol transport model and the assimilation of aerosol optical depth with

109   MODIS. We then compare MATCH AOD to MODIS and MERRA2 aerosol products, as

110   well as to AOD from the Aerosol Robotic Network (AERONET, Holben et al. 1998).

111   Section 3 discusses differences found between the various estimates of AOD. Section 4

112   looks at clear sky surface irradiance calculations from the SYN1deg product compared to

113   observed values and the impact of AOD and particle size on the results. Conclusions are

114   presented in section 5.

115

116

2. Description of MATCH model

117

118   The Model for Atmospheric Transport and Chemistry (MATCH) is a transport

119   model of intermediate complexity driven by offline meteorological fields from the

120   National Centers for Environmental Prediction (NCEP) reanalysis. It is run on a 194×96

121   (1.9°×1.9°) spatial grid with a vertical resolution of 28 sigma-p levels. Temporally, the

122   meteorological fields are linearly interpolated to 30-minute times at which time the

123   chemical processes are run. One exception is that the sulfur model is interpolated again to

124   run at 2-min subscale time steps. MATCH is one of the many aerosol transport models

125   that participated in the AeroCom model inter-comparison project (Textor et al., 2006;

126   Kinne et al. 2006; Textor et al. 2007) and the AeroCom carbon inter-comparison project

127   (Koch et al., 2009; Huneeus et al., 2011).

128   Aerosol types included in MATCH are dust, sulfate, sea salt, soot, sulfates,

129   carbon, and volcanic particles (**Table 1**). Model physics included in MATCH are

130   parameterizations for convection and boundary layer processes that include prognostic

131   cloud and precipitation schemes for aqueous chemistry and the scavenging of soluble

132   species. MATCH also includes the ability to resolve the transport of aerosols via

133   convection, boundary layer transport, and scavenging and deposition of soluble gases and

134   aerosols. MATCH can simulate most cloud processes currently in use in a GCM (eg.

135   cloud fraction, cloud water and ice content, fraction of water converted to rain and snow,

136   and evaporation of condensate and precipitate). It also includes vertical turbulent eddy

137   processes. These processes are then used for convective transport, wet scavenging, wet

138   deposition and dry deposition of the MATCH aerosols. These various parameterizations

139   were developed, originally, for the NCAR Community Climate Model (CCM) and

140   subsequently incorporated into the MATCH model. Descriptions of these

141   parameterizations are given by Rasch et. al (1997, 2001), Collins et. al (2001) and

142   additional papers described therein.

143   The MATCH aerosol suite includes a detailed mineral dust scheme in the Dust

144   Entrainment and Deposition model, (Zender et al., 2003), and a diagnostic

145   parameterization for sea-salt aerosol based on the 10m wind speed (Blanchard and

146   Woodcock, 1980). The sulfur cycle and the chemical reactions for sulfate aerosol creation

147   rely on monthly climatological oxidant fields and emission inventories (**Table 1**) for

148   sulfur oxides and oceanic dimethyl sulfide (photochemistry and nitrate aerosol are

149   omitted). The reaction scheme is similar to that of the Model for Ozone and Related

150   Chemical Tracers (MOZART), (Emmons et al., 2010). Carbon aerosols (both organic

151   compounds and soot) evolve with simple mean lifetime e-foldings from surface fluxes

152   specified through natural, biomass burning and fossil fuel burning emission inventories

153   (also monthly climatologies given in **Table 1**).

154

Table 1. Aerosol Types & Climatological Sources

Aerosol Type	Source	Description
Sea Salt	Blanchard and Woodcock, 1980	Wind Driven
Dust	Ginoux et al. (2001); Zender et al. (2003)	NCEP soil moisture, wind driven
Sulfate (natural & anthropogenic)	Benkovitz et al. (1996); Barth et al. (2000)	monthly climatological
Carbon (organic & Soot)	Liousse et al. (1996)	monthly climatological
Volcanic	Episodic inclusion of Sulfur dioxide	Processed by model

155

156   The optical properties of the various aerosol types (e.g. mass extinction

157   coefficient, single scatter albedo), which are key parameters for aerosol assimilation, are

158   drawn from the standard Optical Properties of Clouds and Aerosols (OPAC, Hess et al.

159   1998) database. However, scattering properties of maritime and dust aerosols used

160   in the radiative transfer calculations in the SYN1deg are not from MATCH. Instead,

161   aerosol types from MATCH are mapped to a similar set of scattering properties, per

162   Table 2, embedded in the Langley Fu & Liou radiative transfer (LFLRT) code (Fu and

163   Liou, 1993; Fu et. al 1998; Rose et. al 2013). These include OPAC as in MATCH for all

164   but the small and large dust particles. Dust scattering and absorption properties in the

165   LFLRT code are from Sinyuk et al. (2003).

166

Table 2. Mapping of MATCH aerosol types into Radiative Transfer code.

MATCH Constituent	Langley Fu & Liou Constituent	Langley Fu & Liou Spectral Properties
Sea Salt	Maritime	d'Almeida 1991
Hydrophobic Organic Carbon	Insoluble	OPAC
Hydrophilic Black Carbon Hydrophobic Black Carbon	Soot	OPAC
Hydrophilic Organic Carbon Tropospheric Sulfate	Water Soluble (WASO)	OPAC
Volcanic Stratospheric Sulfate	Suspended Organic (SUSO)	OPAC
Dust < 1.0µm	"Small" Dust	Sinyuk et al. (2003)
Dust 1.0 -2.5µm Dust 2.5-5.0 µm Dust 5.0-10.0 µm	"Large" Dust	Sinyuk et al. (2003)

167

168   **Figure 1** shows the single scatter albedo (SSA) and asymmetry parameter (ASY)

169   for the seven constituents in the LFLRT code at 500µm. Constituents with constant SSA

170   and/or ASY are given as numbers while those that vary with relative humidity are

171   plotted. The spectral properties for sea salt shown in Figure 1 were taken directly from

172   tables in d'Almeida et al., (1991). Note that the asymmetry parameter of maritime

173   aerosol decreases with humidity. This is likely an error in the original Table A.30 of

174   d'Almeida et al. (1991).
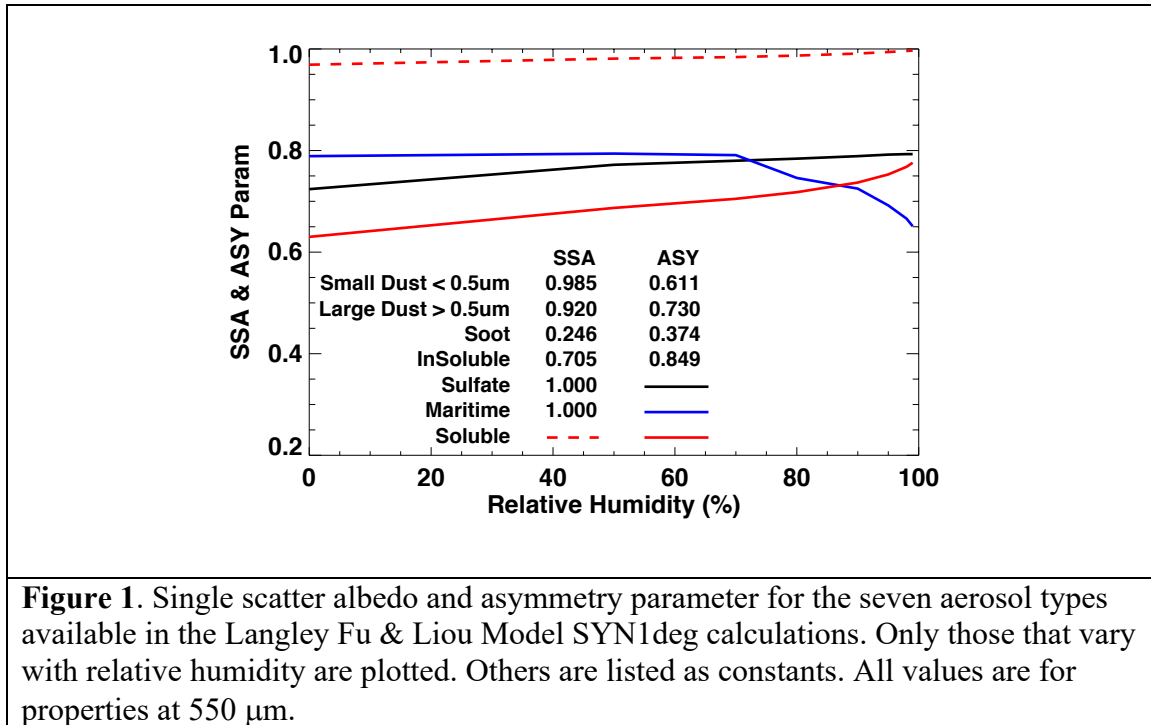
Figure 1. Single scatter albedo and asymmetry parameter for the seven aerosol types available in the Langley Fu & Liou Model SYN1deg calculations. Only those that vary with relative humidity are plotted. Others are listed as constants. All values are for properties at 550 μm.

175

176   **2.1 MATCH Assimilation of MODIS Aerosol Optical Depths**

177   One major advantage of the MATCH model is its ability to reliably assimilate

178   satellite-based retrievals of aerosol optical depth (AOD) to constrain the climatologically

179   forced aerosols generated within the chemical transport portion of the code. Edition 4

180   MATCH algorithms ingest MODIS Collection 6.1 AOD (Remer et al., 2005), beginning

181   in March 2000 from the Terra satellite and June 2002 from both Terra and Aqua

182   satellites. The MATCH assimilates MODIS AOD at the green wavelength of 550 nm.

183   MATCH combines AOD derived by the Dark Target (Levy et al. 2013) and Deep Blue

184   algorithms (Hsu et al., 2006). A global daily mean AOD in a 1.9°x1.9° grid is derived

185   from Terra and Aqua observations by simply averaging available Terra and Aqua dark

186 target and deep blue derived AODs in a grid box. Unlike dark target and deep blue

187 merged product (MOD08), we do not use a quality assurance confidence (QAC) score to

188 screen AOD.

189   The assimilation process begins by combining the dark target and deep blue AOD

190 from MODIS (both Terra and Aqua when available) and creating daily averages. As

191 MATCH progresses through time the AOD at local solar noon are assimilated by taking a

192 15° longitude width of retrieved AOD from the daily mean map. Examples of the

193 magnitude of AOD adjustments by the assimilation are shown in **Fig. 2. Figure 2a** shows

194 hourly AOD field differences, 4 UT minus 3 UT on February 1st, 2020. Similarly, **Figure**

195 **2b** shows 10 UT minus 9 UT of the same day. The 15° vertical band is clearly visible

196 where red (blue) colors indicate total column aerosol is increased (decreased) by the

197 MODIS AOD assimilation. Following the AOD adjustment, aerosol masses in the

198 atmospheric column through the troposphere are scaled to closely match the AOD

199 derived from MODIS. Neither the vertical profile nor the relative abundance of the

200 aerosol species is adjusted. Once aerosol mass is adjusted at the local noon for the regions

201 where MODIS AOD is available, the adjusted aerosol mass is carried on to the next time

202 step. Besides the MODIS adjustments, wind driven sea-salt creation and deposition are

203 found along frontal boundaries in the North Atlantic and Southern Oceans. The maps also

204 indicate hourly increases and decreases in high aerosol loading areas such as those found

205 around China and SE Asia. Episodic events such as intense fires or volcanic eruptions

206 are not specifically included in the MATCH aerosol package. Such events are captured

207 by the assimilation of MODIS AOD and total column aerosol loading is adjusted upward.

208 The adjustment is applied to AOD only. The aerosol type (and so scattering properties) is

209   not adjusted to reflect the reality of the scattering or absorbing aerosol during such an

210   event.

Figure 2. Difference of MATCH AOD due to the assimilation of MODIS AOD. The left plot is 4 UT minus 3 UT and right plot is 10 UT minus 9 UT on February 1, 2020. AOD is adjusted at the local solar noon within the 15° longitudinal band by the MODIS AOD assimilation. Wind-blown dust and sea salts differences are also apparent outside the 15° longitudinal band.
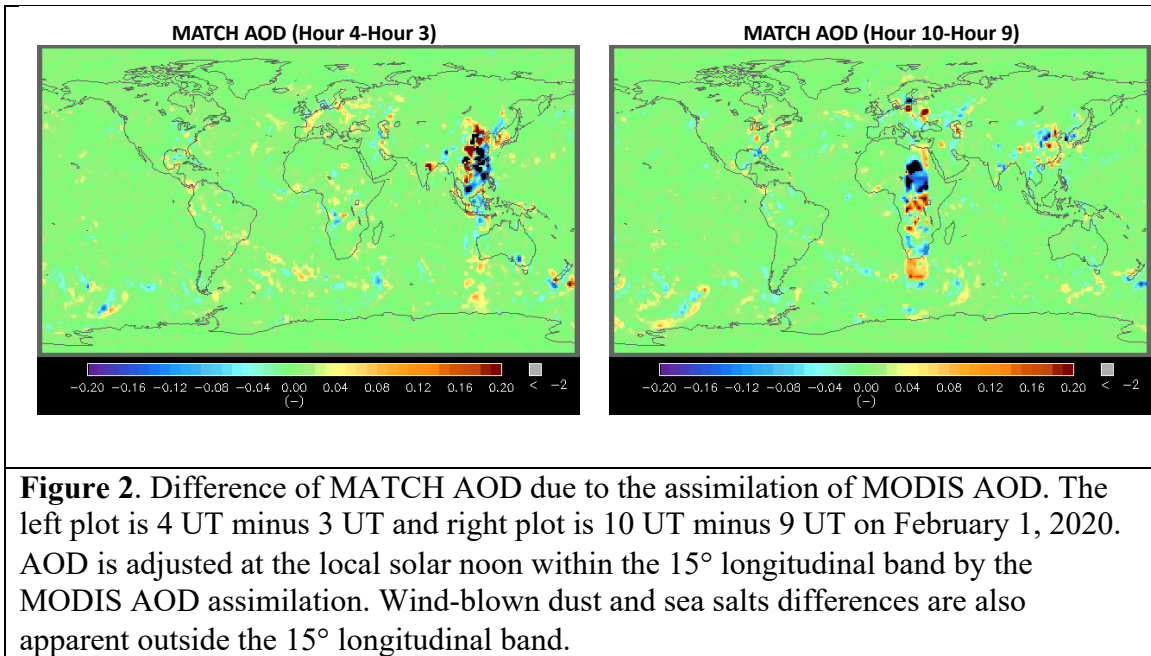
211

212   **2.2 MATCH and MERRA2 comparison**

213   In this section, we compare AODs between MATCH and MERRA2 (Randles et

214   al., 2017) in which MODIS clear-sky radiances are assimilated. MERRA2 also

215   assimilates surface observed AOD by AERONET and ship born AOD observations as

216   well as AVHRR and MISR retrievals for the years 2000-2002 and 2000-2014

217   respectively. We compare AODs in two different ways. First, MATCH and MERRA2

218   AODs are compared with MODIS AODs. The first comparison tests the consistency of

219   daily means when MODIS aerosol optical depth is available (i.e. clear somewhere in the

220   grid box at Terra and Aqua overpass time). Second, MATCH and MERRA2 AODs are

221   compared under all-sky conditions, which is only possible with modeled AODs.
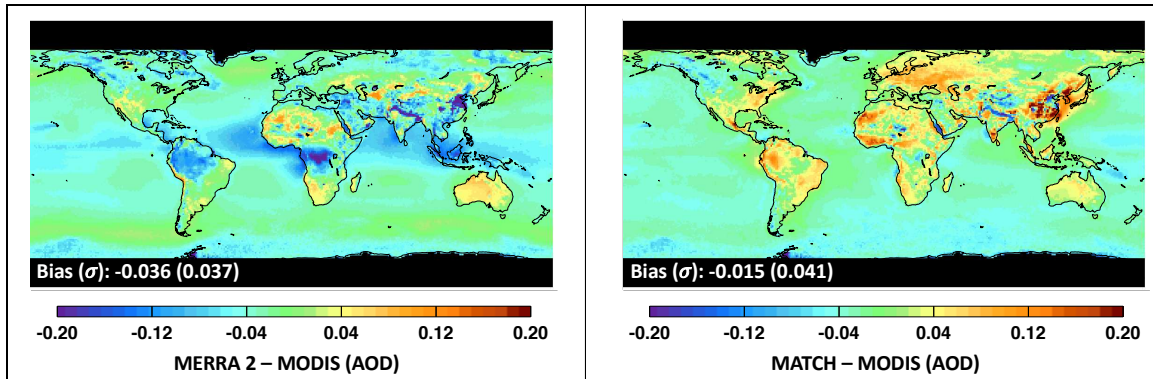
Figure 3: Climatological mean aerosol optical depth (AOD, i.e. $\langle AOD_{MODIS}^{clr} \rangle$ see texts for the definition) difference of left) MERRA2 – MODIS and right) MATCH – MODIS averaged over Mar 2000 through Feb 2020. MERRA2 and MATCH daily mean AODs are sampled when daily mean MODIS AOD from the same 1°×1° grid is available. Sampled daily mean AODs are subsequently averaged. MODIS AODs are averages of MODIS dark target and deep blue algorithms from both Terra (MOD08) and Aqua (MYD08) data products.

222

223   **Figure 3** shows differences of climatological mean AOD between MERRA2 and

224   MODIS on the left and MATCH and MODIS on the right. To compute the monthly mean

225   AOD differences, both MERRA2 and MATCH daily mean AODs are sampled when

226   daily mean MODIS AOD (MODIS products MOD08 and MYD08) from the same 1°×1°

227   grid is available (hereinafter AOD_{MODIS}^{clr}). Sampled daily mean AODs (AOD_{MODIS}^{clr}) are

228   subsequently averaged (hereinafter $\langle AOD_{MODIS}^{clr} \rangle$, where the bracket indicates a simple

229   arithmetic mean). Although both products assimilate MODIS observations, each shows

230   fairly significant differences from MODIS values. Differences arise because MODIS

231   daily mean AOD is clear sky at Terra and Aqua overpass time while MERRA2 and

232   MATCH daily mean AOD includes AOD from other times of the day. When the non-

233   overpass time is also clear, MATCH AOD_{MODIS}^{clr} should be close to MODIS AOD_{MODIS}^{clr}.

234   However, when clouds are present in MATCH during non-overpass times, modeled AOD

235   are used, hence the daily mean AOD can deviate from MODIS AOD_{MODIS}^{clr}. In addition,

236 AOD differences for MERRA2 at Terra and Aqua overpass times might be larger than

237 MATCH even for clear-sky conditions as MERRA2 assimilates observed AOD data

238 other than MODIS AOD when and where these events might occur.

239   While MATCH shows large positive differences over land, especially China and

240 southeast Asia, Australia, Amazon, and north Africa, MERRA2 shows significant

241 negative differences over major rain-forest regions of south America, Africa, and the

242 tropical western Pacific. Both products are closer to MODIS AOD over ocean compared

243 to $\langle AOD_{MODIS}^{clr} \rangle$ over land except MERRA2 shows a negative difference across the Indian

244 ocean and off the west coast of Africa in the Atlantic Ocean. When MODIS AOD_{MODIS}^{clr} is

245 available in the grid box, MATCH weighs MODIS AOD heavily in its assimilation at

246 local solar noon so that MATCH AOD is nearly identical to MODIS AOD at the local

247 noon under clear-sky regions. Consequently, the difference of climatological global mean

248 MATCH and MODIS AOD_{MODIS}^{clr} (-0.015) is smaller than the difference of MERRA2 and

249 MODIS AOD_{MODIS}^{clr} (-0.036).

250   **Figure 4** shows the difference of AOD_{MODIS}^{clr} more clearly. In **Fig. 4** AOD_{MODIS}^{clr} are

251 compared directly in a log-density plot where each point represents a comparison for the

252 daily average of a given grid box; MERRA2 versus MODIS on the left and MATCH

253 versus MODIS on the right. **Figure 4** indicates that MATCH AOD_{MODIS}^{clr} has a smaller

254 bias with respect to the MODIS AOD than the MERRA2 AOD but has approximately the

255 same RMS compared to the MERRA2 AOD_{MODIS}^{clr}.

256

257
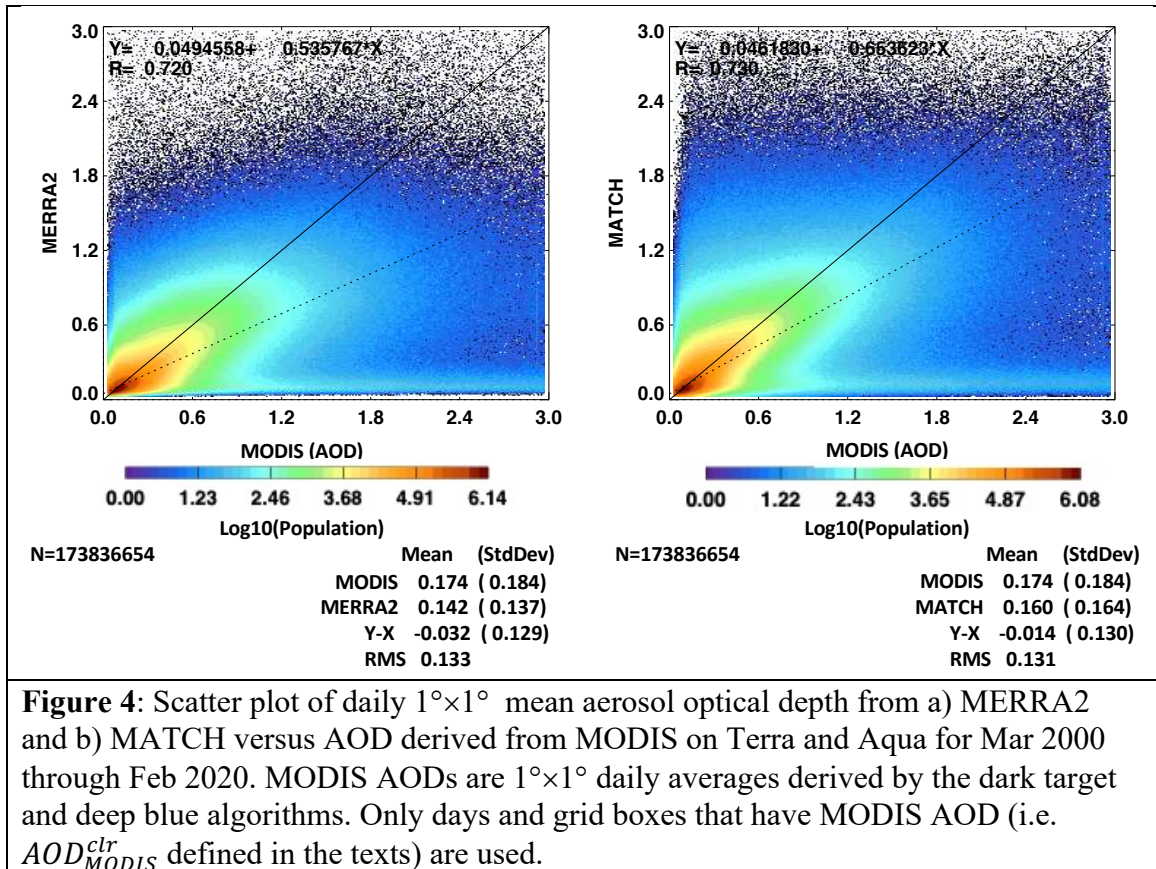
Figure 4: Scatter plot of daily 1°×1° mean aerosol optical depth from a) MERRA2 and b) MATCH versus AOD derived from MODIS on Terra and Aqua for Mar 2000 through Feb 2020. MODIS AODs are 1°×1° daily averages derived by the dark target and deep blue algorithms. Only days and grid boxes that have MODIS AOD (i.e. AOD_{MODIS}^{clr} defined in the texts) are used.

258
259
260   We now consider more directly, differences between the MATCH and MERRA2

261   climatological AOD fields for all-sky and *estimated* clear sky conditions. **Figure 5** shows

262   1°×1° climatological mean maps of MATCH AOD on the left and its difference from

263   MERRA2 on the right for all sky (top maps) and estimated clear sky (bottom maps)

264   conditions for March 2000 through February 2020. A clear-sky area weighted monthly

265   mean aerosol optical depth is derived by averaging daily mean aerosol optical depth

266   weighted by clear fraction (hereinafter $\overline{AOD_{MODIS}^{clr}}$, overbar indicates monthly mean),

267   where the clear fraction is derived from MODIS on Terra and Aqua (Loeb et al. 2020,

268   Minnis et al. 2020). MATCH all-sky AOD (hereinafter $\overline{AOD^{all}}$) is larger than MERRA2

269    $\overline{AOD^{all}}$), particularly over the rain forest regions of the globe as well as India and China.

270   Although the difference is smaller, the difference of $\overline{AOD_{MODIS}^{clr}}$ shows a similar spatial

271   pattern (**Fig. 5** bottom right) to the all-sky difference. This is consistent with **Fig. 3**,

272   showing that MERRA2 AOD_{MODIS}^{clr} underestimates AOD with respect to MODIS

273   AOD_{MODIS}^{clr}. A larger difference in MATCH AOD over convective regions (e.g. Amazon,

274   central Africa, and south east Asia) is caused by how dark target and deep blue AOD are

275   merged. As mentioned earlier, we do not use QAC to screen AOD. Convective clouds

276   introduce a larger uncertainty to AOD because of a 3D radiation effect or poor fit to

277   observations with retrieved AOD (personal communication with R. Levy 2020). For

278   these situations, AODs associated with QA confidence scores less than 2 are screened out

279   in the MOD08 dark target and deep blue merged product (Levy et al. 2013).

280   **2.3 Comparison with AERONET**

281   The above results indicate that both MATCH AOD_{MODIS}^{clr} and MERRA2

282    $\overline{AOD_{MODIS}^{clr}}$ are generally smaller than MODIS $\overline{AOD_{MODIS}^{clr}}$. Larger difference between

283   MATCH and MERRA2 $\overline{AOD^{all}}$ over convective regions originated from merged AOD

284   product used for the assimilation. Of primary importance to radiative transfer calculations

285   within the SYN1deg product is the ability of the MATCH model to accurately represent

286   total column aerosol optical depth. To test the overall accuracy, we use observations from

287   the AERosol RObotic NETwork (AERONET). AERONET is a global federation of

288   ground-based remotes sensing sites developed by NASA and now supported by a number

289   of institutions around the world (Holben et al. 1998). Each site maintains a CIMEL sun-

290   photometer that scans the daytime sky every 20 minutes. Collected data are processed

291   according to standards of calibration and processing maintained by the AERONET

292 project. Here we utilize Level 2.0, data that have been screened for clouds and quality

293 assured (Smirnov et al. 2000).

294

Figure 5. Left) Climatological mean AOD from MATCH and right) the difference between MATCH and MERRA2 (MATCH – MERRA2). Top maps are for all-sky (AOD_{MODIS}^{all}), bottom maps are clear-sky area weighted average of AOD (AOD_{MODIS}^{clr}). Clear-sky weighted monthly mean AOD is derived by averaging daily mean aerosol optical depth weighted by daily 1°×1° gridded mean clear fraction where the clear fraction is derived from MODIS based cloud fraction on Terra and Aqua.

295

296   **Figure 6** shows an hourly time series of AOD from MATCH, MERRA2 and

297 AERONET for January 2010 at the Beijing China AERONET site. The top plot shows

298 cloud fraction time series derived from MODIS and GEOs from the SYN1deg Ed4.1

299 product (Rutan et al. 2015), and the bottom plot shows AOD time series. Generally, both

300 models produce a large variability of AOD at this site fairly well over the course of the

301   month. While both MERRA2 and MATCH AODs increase near times when cloud

302   fraction approaches 100%, the increase of MATCH AOD, which correlates with the

303   increase of AERONET AOD relatively well, is larger than the increase of MERRA2

304   AOD. Although the temporal correlation coefficient of the MATCH and AERONET

305   AODs is smaller at this site during summer months than during winter months (not

306   shown), a good temporal correlation between MATCH and AERONET AODs is

307   consistent across most locations and times we considered. To show this statistically, in

308   the following, we extend this analysis to a number of AERONET sites grouped

309   geographically based on general aerosol type.

310
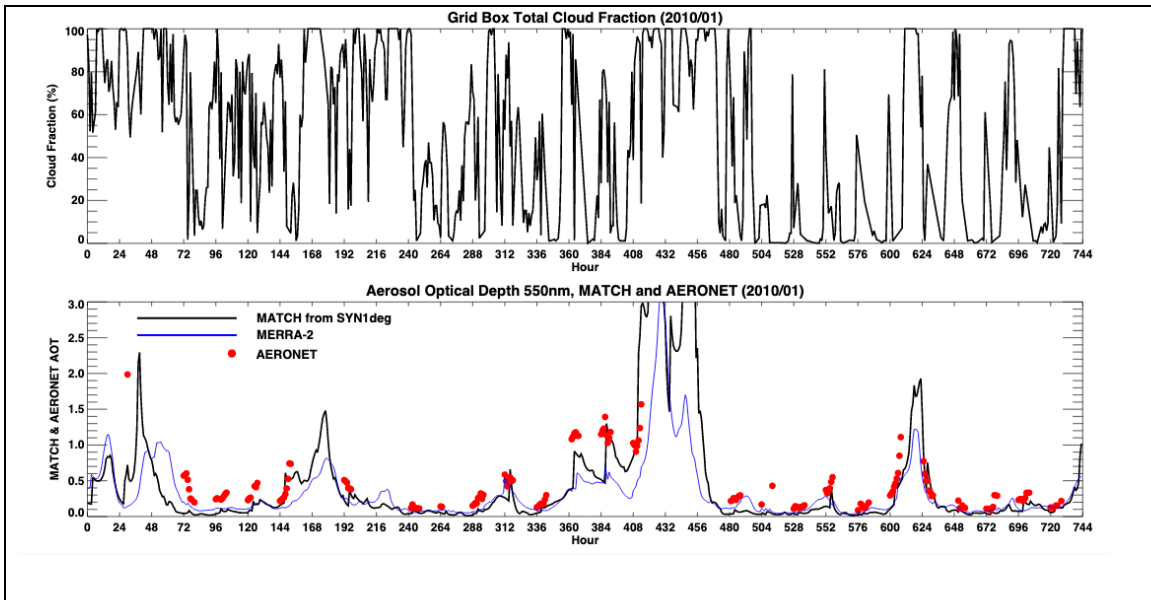
Figure 6. Hourly time series of grid box cloud fraction (top) from SYN1deg Ed4.1
CERES product and AOD (bottom). Results are from the grid box containing the
AERONET Beijing, CH site. Black line MATCH, blue line MERRA-2, red dots,
AERONET observations. MATCH and, to a lesser degree MERRA-2 often have large
increases in AOD when cloud fraction nears 100%.

311

312   Aerosol optical depths from AERONET are nominally provided at 8 spectral

313   channels, every 20 minutes given favorable conditions. We use two channels to derive

314   observed AOD at 550 nm to compare to the AOD provided by the MATCH model.

315   Because the SYN1deg radiative transfer calculation is done hourly, we average any

316   observations within a given hour period centered at the 30th minute for each site

317   collocated within a SYN1deg grid box. AERONET sites chosen are shown in **Figure 7**

318   with a complete listing of all sites in Appendix 1. Though we examine 55 sites over 20+

319   years, we aggregate the statistics within continental regions which naturally isolates them

320   by general climatic conditions. Tables 3 and 4 show comparisons for each site grouping,

321   respectively, for clear sky (less than 1% cloud identified by MODIS and geostationary

322   satellites in the SYN1deg grid box) conditions and for all sky (any cloud condition within

323   the SYN1deg grid box) conditions. Using clear-sky scenes identified by MODIS only

324   gives the same statistical results with fewer number of samples. Statistics shown in

325   Tables 3 and 4 are the average observed value, mean bias (MATCH – Observation), root

326   mean square (RMS) difference and the correlation coefficient (R) over the time period

327   from March 2000 through February 2020. The actual time period varies depending on the

328   site due to AERONET data availability. The RMS difference and correlation coefficient

329   are computed by each site with hourly mean values where observations are available

330   from March 2000 through February 2020. For comparison purposes we show the same

331   statistics derived from observations compared to MERRA2 AODs using the identical

332   hours. We note, however, that MERRA2 assimilates AERONET while MATCH AODs

333   are independent from AERONET AODs. MATCH AOD for the Brazil group is biased

334   high by 0.02, and the China/Korea group has no appreciable bias compared with

335   AERONET AODs. These two regions have relatively large bias of $\langle AOD_{MODIS}^{clr} \rangle$ from
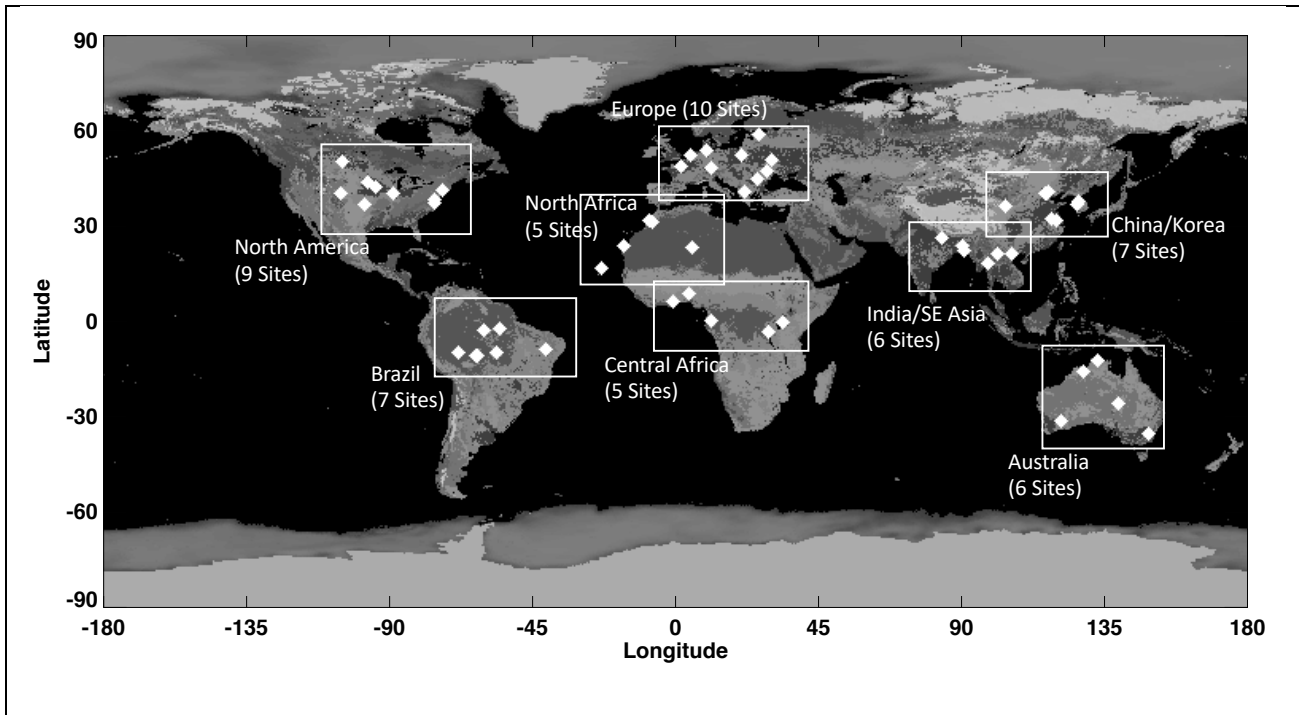
Figure 7. Location of AERONET sites and how they grouped for calculations of mean/bias/RMS with respect to MATCH and MERRA-2 optical depths found in tables 3 and 4.

336

337   MATCH compared with MODIS AODs (**Fig. 3** right). In contrast, negative bias of

338   MERRA2 AODs compared with AERONET AODs for Brazil, central Africa, and

339   China/Korea groups are consistent with negative bias of MERRA2 $\langle AOD_{MODIS}^{clr} \rangle$

340   compared with MODIS AODs (**Fig. 3** left). For the China/Korea group, the RMS

341   difference between MATCH AODs and AERONET AODs is 0.18 and correlation

342   coefficient is 0.7. These are worse than the counterpart values of MERRA2 versus

343   AERONET AODs because summertime agreement between MATCH and AERONET

344   AODs is worse if a similar plot as **Fig. 6** is plotted for summertime when hygroscopic

345   aerosols are dominant under high relative humidity conditions.

346   The sign of the MATCH AODs compared to AERONET AODs for all-sky

347   conditions is generally consistent with the sign of clear-sky counterparts. The RMS

348   difference under all-sky conditions is generally larger than the clear-sky RMS difference

349 while the correlation coefficient is nearly the same. The biases for MERRA2

350 comparisons are generally comparable to MATCH though RMS for MERRA2 tend to be

351 slightly smaller and correlations tend to be higher due in part to the assimilation of

352 AERONET into the MERRA2 model.

353

Table 3. Hourly AERONET station statistics for MATCH and MERRA-2.
Continental Groups, Clear Sky conditions[1]

Site	Predominant Aerosol Type	Number	Observed Average	MATCH			MERRA-2		
				Bias	RMS	R^2	Bias	RMS	R^2
Australia (5 Sites)	Dust Smoke	20925	0.06	0.01	0.06	0.4	0.03	0.05	0.7
Brazil (7 Sites)	Smoke Polluted	6554	0.14	0.02	0.10	0.8	-0.02	0.08	0.9
Central Africa (5 Sites)	Smoke	2139	0.70	-0.10	0.24	0.9	-0.10	0.24	0.9
North Africa (5 Sites)	Dust	10047	0.17	0.07	0.15	0.7	0.02	0.10	0.8
China/Korea (8 Sites)	Polluted	2827	0.26	-0.00	0.18	0.7	-0.03	0.15	0.8
India/SE Asia (6 Sites)	Smoke Polluted	3010	0.51	-0.09	0.28	0.6	-0.10	0.24	0.8
North America (9 SItes)	Continental Polluted	21429	0.10	-0.00	0.07	0.7	0.00	0.06	0.8
Europe (10 Sites)	Continental Polluted	10211	0.13	0.01	0.07	0.7	-0.02	0.05	0.8
[1]The time period used is from Mar 2000 through Apr 2020. Actual period varies by site depending on AERONET data availability. Clear Sky is identified by MODIS and geostationary satellites and the cloud fraction is less than 1% over a SYN1deg grid box.									

354

355 Results for all points across all sites and times are shown in **Figure 8**. The color density

356 plots are in log scale and indicate the vast majority of observations have an AOD of less

357 than one for both clear and all sky conditions observed within the SYN1deg grid box.

358 Biases are less than 10% of the mean value but RMS is large relative to the mean

359 observed value. Overall correlation is approximately 0.8. The 'clear sky' hours (where

360 SYN1deg estimated less than 1% cloud in the grid box based on MODIS and GEO

361 observations) is a little more than 10% of the overall points. When MATCH AOD is

362 compared to MERRA2 AOD (not shown) MATCH is biased approximately 10% higher.

363

Table 4. Hourly AERONET station statistics for MATCH and MERRA-2.
Continental Groups, All Sky Conditions[1]

Site	Predominant Aerosol Type	Number	Observed Average	MATCH			MERRA-2		
				Bias	RMS	R^2	Bias	RMS	R^2
Australia (5 Sites)	Dust Smoke	110523	0.09	0.00	0.09	0.5	0.02	0.07	0.8
Brazil (7 Sites)	Smoke Polluted	72656	0.25	0.03	0.23	0.8	-0.04	0.18	0.9
Central Africa (5 Sites)	Smoke	41193	0.55	-0.07	0.26	0.8	-0.10	0.26	0.9
North Africa (5 Sites)	Dust	43205	0.23	0.08	0.20	0.7	0.01	0.14	0.8
China/Korea (8 Sites)	Polluted	52287	0.45	0.01	0.31	0.7	-0.08	0.27	0.8
India/SE Asia (6 Sites)	Smoke Polluted	44534	0.61	-0.06	0.32	0.6	-0.10	0.32	0.7
North America (9 Sites)	Continental Polluted	160356	0.13	0.02	0.13	0.6	0.00	0.09	0.7
Europe (10 Sites)	Continental Polluted	175010	0.18	0.04	0.14	0.6	-0.02	0.08	0.8

[1] The time period used for the statistics is from March 2000 through April 2020. Total sample varies by site depending on AERONET data availability.

364

365 **3. Discussion of AOD Differences**

366   In this section, we investigate the reason for the AOD differences shown in the

367 previous section. In addition, we estimate the effect of the AOD differences to surface

368 irradiances when MATCH AODs are used for surface irradiance computations.

369 Generally, cloud contamination in MODIS AODs is caused by unresolved sub-pixel scale

370 clouds (Kaufman et al. 2005; Martins et al. 2002). The difference shown over convective

371 regions, therefore, seems to be caused by the uncertainty due to 3D radiative effects that

372 impact retrieved AODs by unknown amounts (Wen et al. 2007), by errors in estimating

Figure 8. All sky (left) and clear sky (right) comparisons of observed (AERONET) hour mean optical depths to estimates from the MATCH model for 20+ years at 55 AERONET sites shown in **Fig 7**.
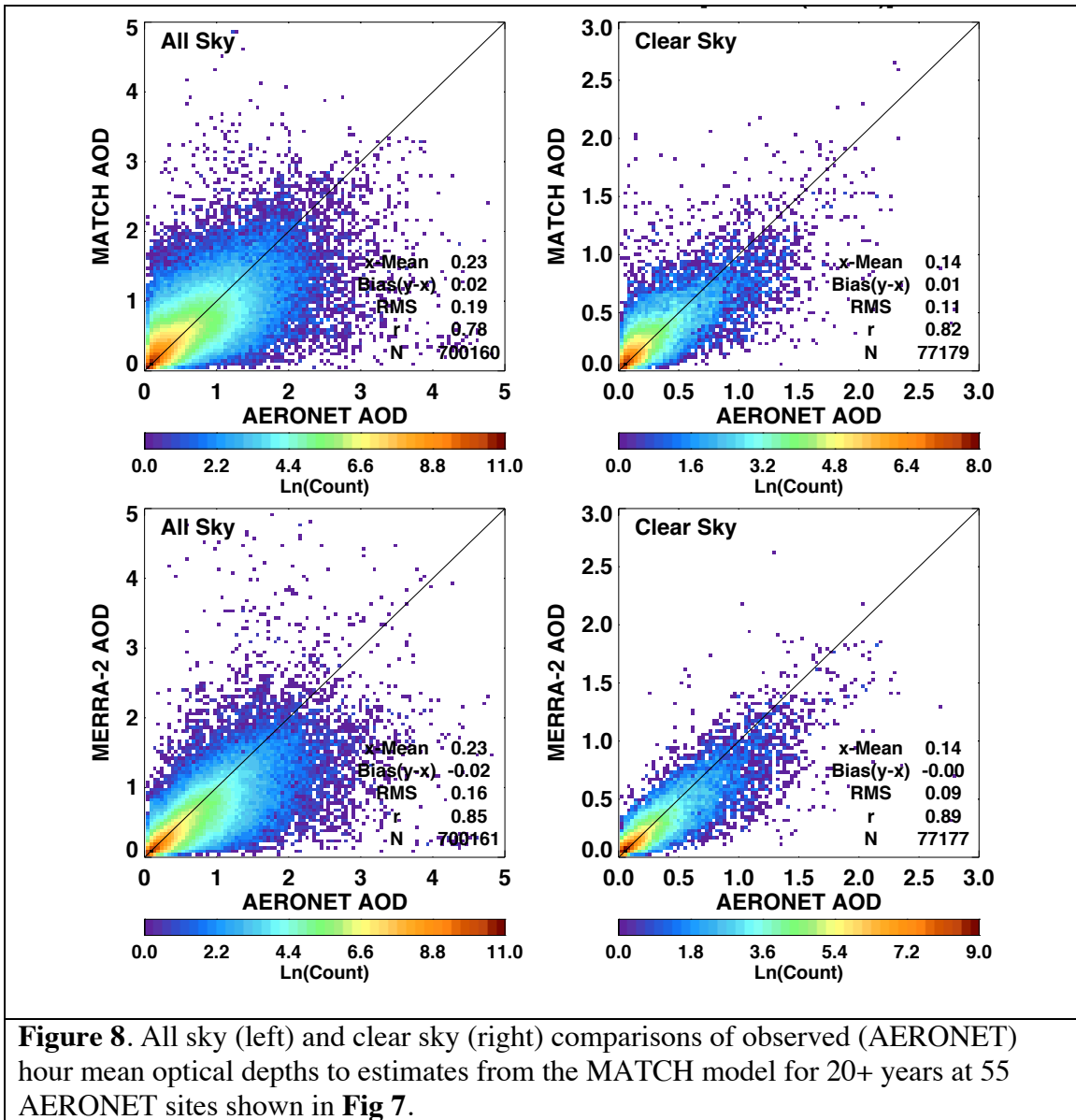
373

374   the fraction of hygroscopic aerosols or by the errors in estimating water uptake by

375   hygroscopic aerosols (Su et al 2008, Marshak et al., 2021). Larger AODs are screened out

376   in the MOD08 data product while the CERES team uses all retrieved AODs regardless of

377   the QAC score, likely increasing MATCH AOD overall. The comparison with

378   AERONET AODs is not decisive to determine how to screen MODIS AODs because

379   MATCH AODs are positively biased and MERRA2 AODs are negatively biased for the

380   Brazil group. The result underscores the difficulty of deriving accurate AODs, which

381   appear to involve requirements in addition to identification of clear-sky scenes. Levy et

382   al. (2013) list reasons lowering the QAC score as 1) pixels are thrown out due to cloud

383   masking, 2) retrieval solution does not fit the observation well, and 3) the solution is not

384   physically plausible given the observed situation. Therefore, even though the difficulty of

385   identifying clear-sky scenes is driven by cloud contamination by trade cumulus (Loeb et

386   al. 2018), the difficulty of deriving AODs exists over convective regions (Varnai et al.,

387   2017) as well.

388   Larger positive biases of MATCH AODs compared with AERONET AODs exist

389   over Africa (Tables 3 and 4). For North Africa, the bias is known to be caused by

390   excessive dust generated by the MATCH algorithm. Even though modeled aerosols are

391   not often used over north Africa owing to the abundance of clear-sky conditions, the dust

392   problem leads to a larger positive AOD bias. In addition, MATCH uses fixed aerosol

393   sources in time. Therefore, it tends to miss large aerosol events, such as forest fires, until

394   clear-sky conditions occur, allowing observations of the event by MODIS. This leads to a

395   larger RMS difference and lower correlation coefficient with AERONET AODs

396   compared with those from MERRA2 versus AERONET.

397   Because MODIS AOD are not generally available under overcast conditions, the

398   reliance on modeled AOD increases as the cloud fraction over a 1°×1° grid increases.

399   **Figure 6**, which shows that AERONET AOD increases with cloud fraction derived from

400   satellites, indicates that as the cloud fraction over a 1°×1° grid increases, AOD over the

401   clear-sky portion of the grid increases. In addition, **Fig. 6** suggests that modeled AODs

402   under near overcast conditions are significantly larger than clear-sky AODs that are

403   constrained by MODIS observations. Because we are unable to evaluate AODs for

404   overcast conditions, here we assess AOD changes with cloud fraction using ground-based

405   observations. **Figure 9** shows the distribution of AERONET AODs for clear-sky and all-

406   sky conditions, as well as precipitable water derived from a microwave radiometer

407   separated by these two conditions. Clear-sky is identified by the Long-Ackerman

408   algorithm (Long et al. 2006) that uses surface direct and diffuse irradiances. **Figure 9**

409   shows that AOD and precipitable water under all-sky conditions are significantly larger
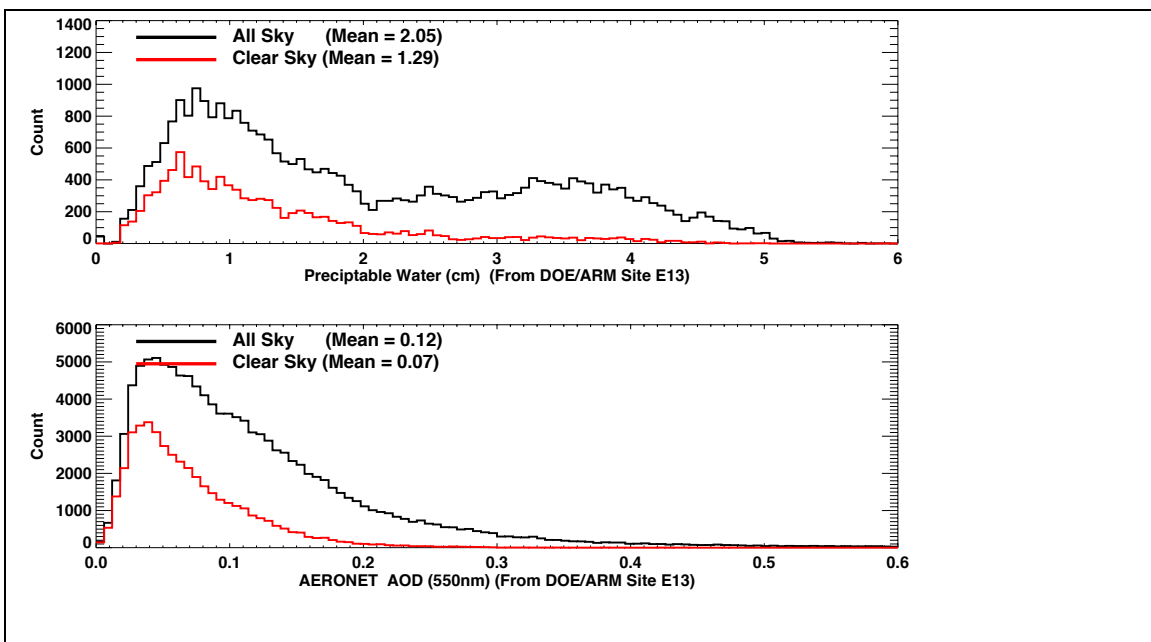
Figure 9. a) 15-minute mean precipitable water distributions from Microwave radiometer observations at ARM/SGP E13 site under all sky and clear sky conditions. b) 15-minute mean aerosol optical depth distributions from AERONET sun-photometer at 550nm. 'Clear sky' is here defined as when a 15-minute time period where the SWFA, surface radiometry-based cloud fraction, equals 0.

410

411   than those under clear-sky conditions. When we use cloud fraction derived from satellite

412   and plot AOD and precipitable water as a function of the cloud fraction using the same

413   grid box where the ground site is located, AOD and precipitable water increase with the

414   cloud fraction (**Fig. 10**). Therefore, increasing AOD with cloud fraction shown in **Fig. 6**

415   is qualitatively explained by increasing AOD of hygroscopic aerosols with relative

416   humidity. However, **Fig. 10** indicates that either the growth of MATCH AOD is too

417   strong or modeled MATCH AOD under all-sky conditions is too large.
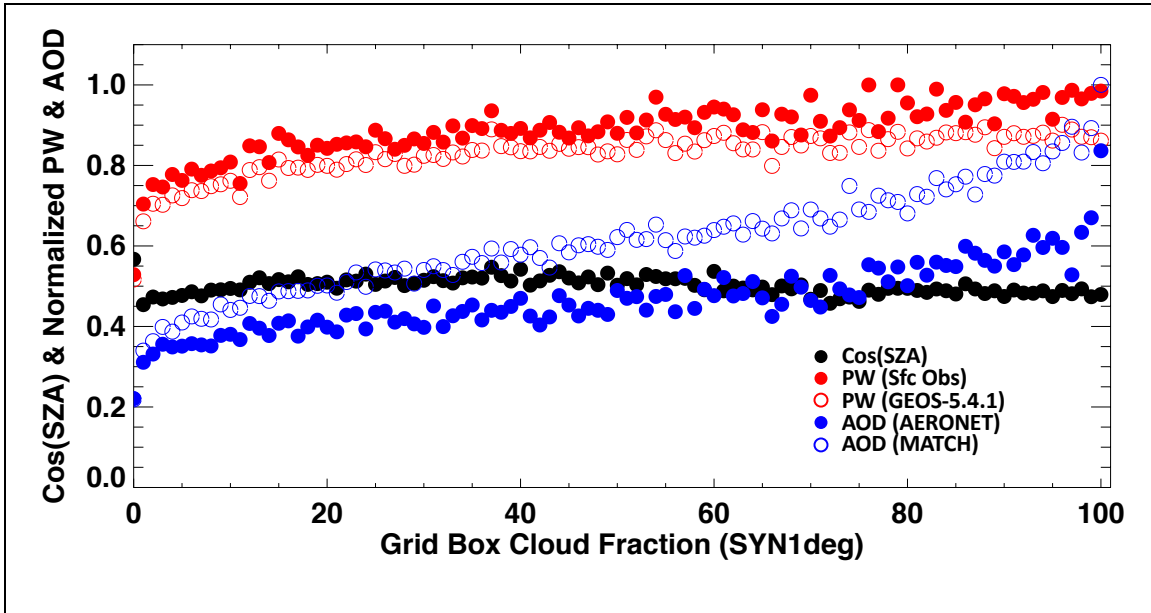
Figure 10. Aerosol optical depth (AOD) and precipitable water (PW) as a function of cloud fraction over the 1°×1° grid box where the ARM/SGP E13 and SURFRAD Bondville IL sites are located. Closed and open blue circles are, respectively, AOD derived from AERONET and MATCH AOD. Closed and open red circles are, respectively, PW derived from microwave radiometer and CIMEL sun photometer and GEOS-5.4.1 PW. Cloud fractions are derived from MODIS and geostationary satellites. Black dots are mean cosine solar zenith angle of the time of AOD and PW observations. AOD and PW are normalized to their maximum value for display.

418

419   **4. Clear Sky Comparisons of SYN1deg and Surface Observed Irradiances**

420   We consider the impact of MATCH aerosols on computed surface irradiances by

421   comparing calculated hourly mean surface downward irradiances from the Ed4.1

422   SYN1deg-Hour product to observations of downward irradiance. In a 1°×1° grid box

423   with an approximate size of 111 km², 100% clear sky sampled over one hour as

424   determined by MODIS or geostationary satellites is relatively rare. None the less, by

425   grouping sites based on general surface conditions and analyzing 20 years of data

426 sufficient samples are found. **Figure 11** shows the sites, grouped by color, including 15

427 land sites labeled "Mid-Latitude" (Green), 6 sites labeled "Desert" (Red), 6 sites labeled

428 "Polar" (White) and 46 buoys (Blue). Surface observed SW irradiance from the land

429 sites comes from the Baseline Surface Radiation Network (Ohmura et al. 1998; Dreimel

430 et al. 2018) and buoy data are made available
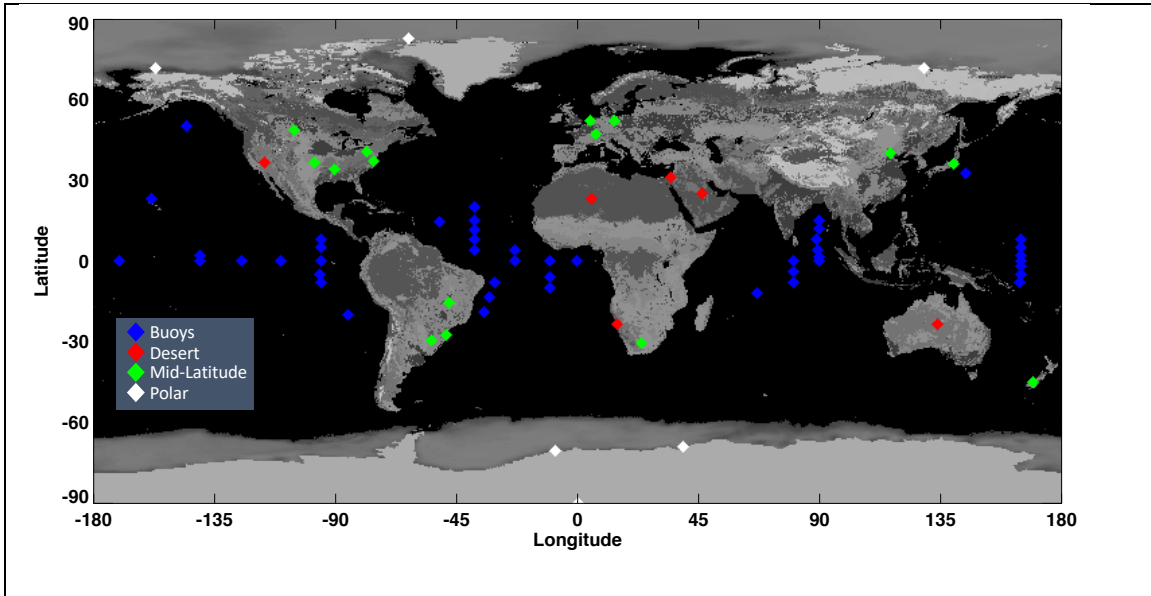
Figure 11. Location of surface observations of downwelling shortwave irradiance used to compare the SYN1deg Ed4.1 calculations to observations for all available hours (from Mar 2000 through Dec 2019) where the SYN1deg cloud analysis determines the hour and grid box to be 100% clear sky.

431

432 from the Pacific Marine Environmental Lab (PMEL) (McPhaden et al. 2002, 2009) and

433 the Woods Hole Oceanographic Institute (WHOI) (Colbo and Weller, 2009). A complete

434 listing is given in Appendix A.

435 **4.1 Shortwave Comparisons**

436 We begin with a simple sensitivity calculation of AOD on surface Downward

437 Shortwave Irradiance (DSI). **Figure 12** shows a series of radiative transfer calculations

438 using the "On-Line Langley Fu & Liou radiative transfer code

439 (https:// cloudsgate2.larc.nasa.gov/cgi-bin/fuliou/runfl.cgi) with an open shrub spectral

440 albedo (broadband albedo of 0.14 at μ_0=1.0), "continental" aerosol, and no clouds.

441 Values on the solid black line are calculated DSI with an AOD of 0.09 at six different

442 solar zenith angles. Calculations were then done for AODs of 0.0 and 0.18, at the same

443 solar zenith angles, representing 100% error bounds of mean AODs derived from

444 AERONET as found in Tables 3 and 4 for the Australia sites where the RMS is

445 approximately equal to the observed average of AOD. Orange and red shaded areas

446 indicate potential bias of DSI at a given solar zenith angle. Irradiance values scale nearly

447 linearly with Cos(SZA) between these limits. **Figure 12** shows the error remains nearly

448 constant until a μ_0=0.5 where it begins to decrease as insolation decreases. However, due

449 to small downward irradiances at large solar zenith angles, the percentage error increases.

450
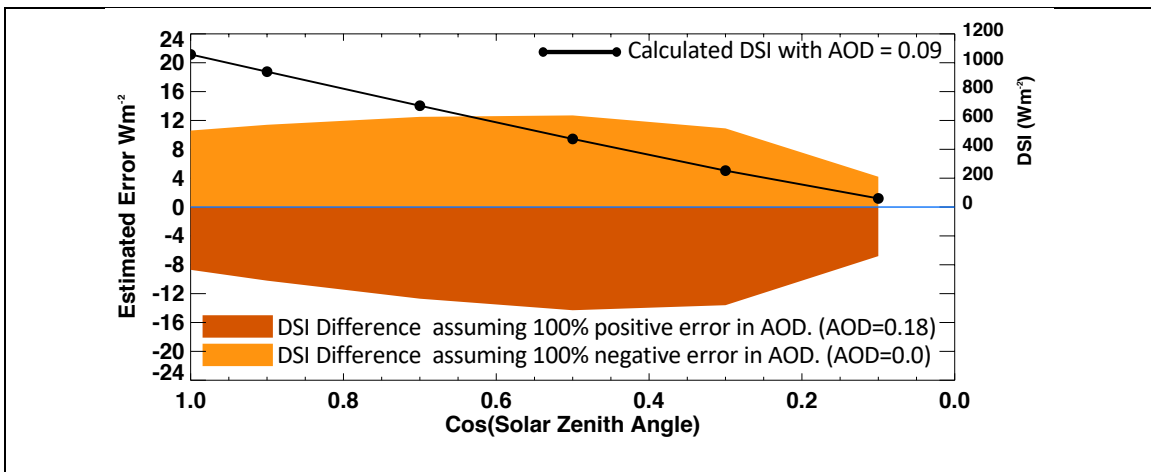
Figure 12. Calculated DSI error at the surface computed with the LFLRT model due to the error in AODs. AOD is assumed to be 0.09. Light and dark orange envelope indicate, respectively, positive and negative errors in Wm-2 (left axis) due to 100% AOD errors. Envelopes are computed with AODs of 0.0 (a -100% error) and 0.18 (a +100% error), at the same solar zenith angles, representing 100% error bounds. Values on the solid black line are calculated DSI (right axis) with an AOD = 0.09 at six solar zenith angles.

451
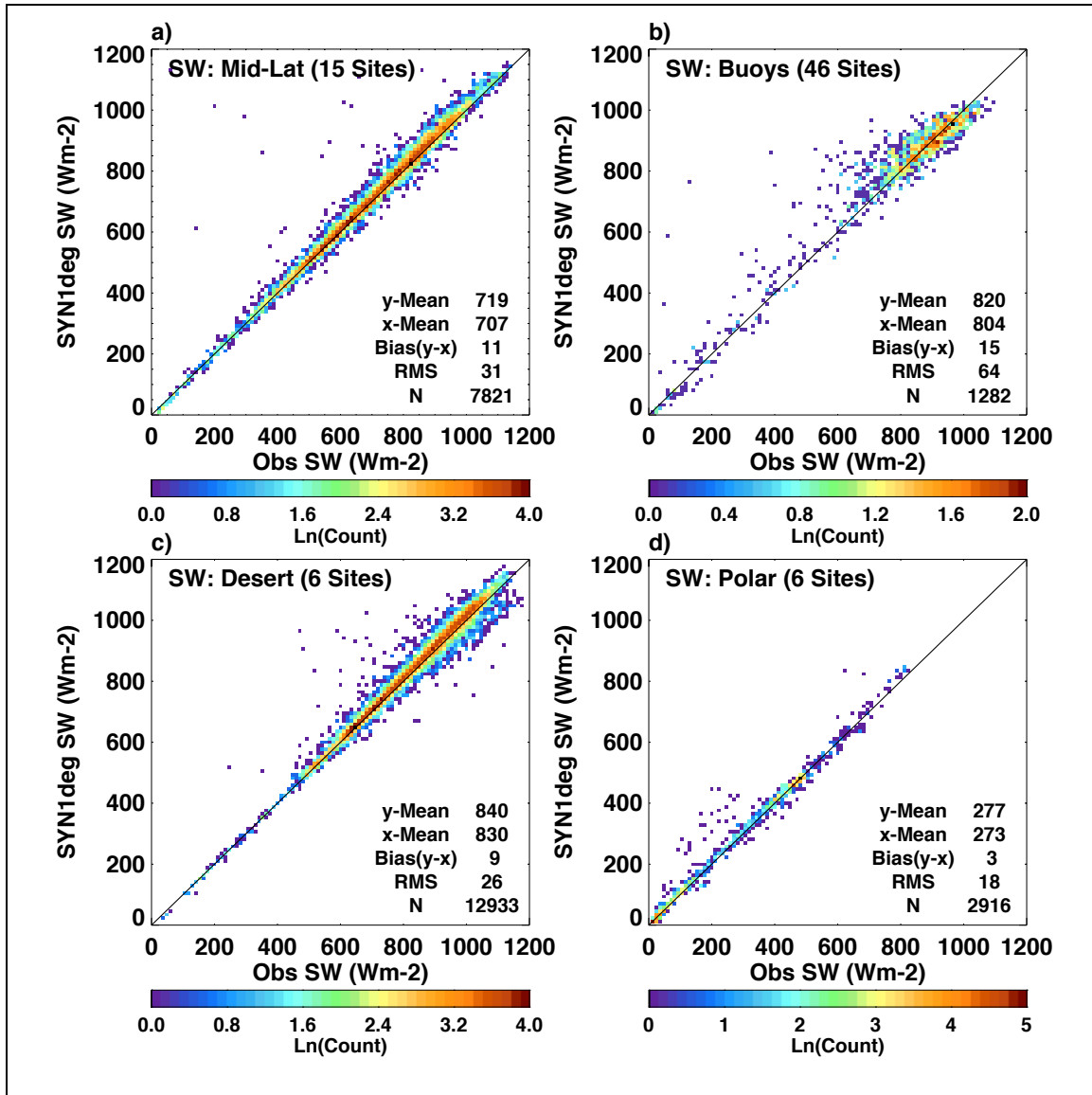
Figure 13. Comparisons of DSI at the surface from the SYN1deg Ed4.1 calculations (y-axis for all plots) and BSRN and buoy surface sites (x-axis all plots). Data are from Mar 2000 through Feb 2020 and only include hours when a 1° grid box is 100% clear sky according to SYN1deg cloud fraction.

452

453   **Figure 13** shows hourly comparisons of computed clear-sky downward

454   shortwave irradiance compared to observations for the groups of sites shown in **Fig. 11**.

455   In general, calculated irradiance is larger than observed. We find that in every grouping,

456   SYN1deg calculations tend to be too transmissive, overestimating DSI by between 3

457   Wm⁻² (polar sites) and 15 Wm⁻² (ocean buoys) with mid-latitude and desert sites each

458   overestimating DSI by ~10 Wm^{-2}. This points to the possibility that MATCH is weighted

459   too far towards scattering aerosols and too few absorbing aerosols.

460   Clear-sky scenes used for **Fig. 13** are those identified by MODIS and

461   geostationary satellites over the 1° grid box where the ground site is located. That is,

462   when satellites did not detect clouds over the one-hour period within the grid box, we

463   compared computed and observed hourly mean downward shortwave irradiances. DSI is

464   nominally measured by a shaded pyranometer combined with the direct insolation

465   measured by a pyrheliometer on a solar tracker. Though satellites may indicate clear,

466   clouds might have been present within the field-of-view of the pyranometer increasing

467   diffuse radiation. This would increase observed DSI, hence modeled irradiance would be

468   smaller. To verify, we used the ground-based cloud screening algorithm developed by

469   Long and Ackerman (Long et al. 2006) to further screen clouds. For the land groupings,

470   Table 5 shows bias (RMS) of the DSI where both satellite and surface based observed

471   cloud fraction equal 0.0. Though mean bias did not change significantly, the RMS in both

472   the Mid-Latitude and Desert sites was reduced by half due to the more stringent cloud

473   screening.

Table 5. Bias (RMS) of clear sky surface shortwave calculation compared to observation[1].
All in Wm^{-2}

Cloud Analysis	Mid Latitude	Desert	Polar
Satellite	11 (31)	9 (26)	3 (18)
Satellite And Surface	11 (16)	8 (15)	4 (19)

[1]Sample is based on 20 years of calculations when either satellite or satellite and surface cloud analysis indicates 0% cloud.

474

475   **4.2 Longwave Comparisons**

476   In this section we consider the implications of errors in AOD and aerosol type on

477 longwave LFLRT calculations as found in the SYN1deg product. **Figure 14** shows

478 SYN1deg surface downward longwave irradiance (DLI) calculations compared to surface

479
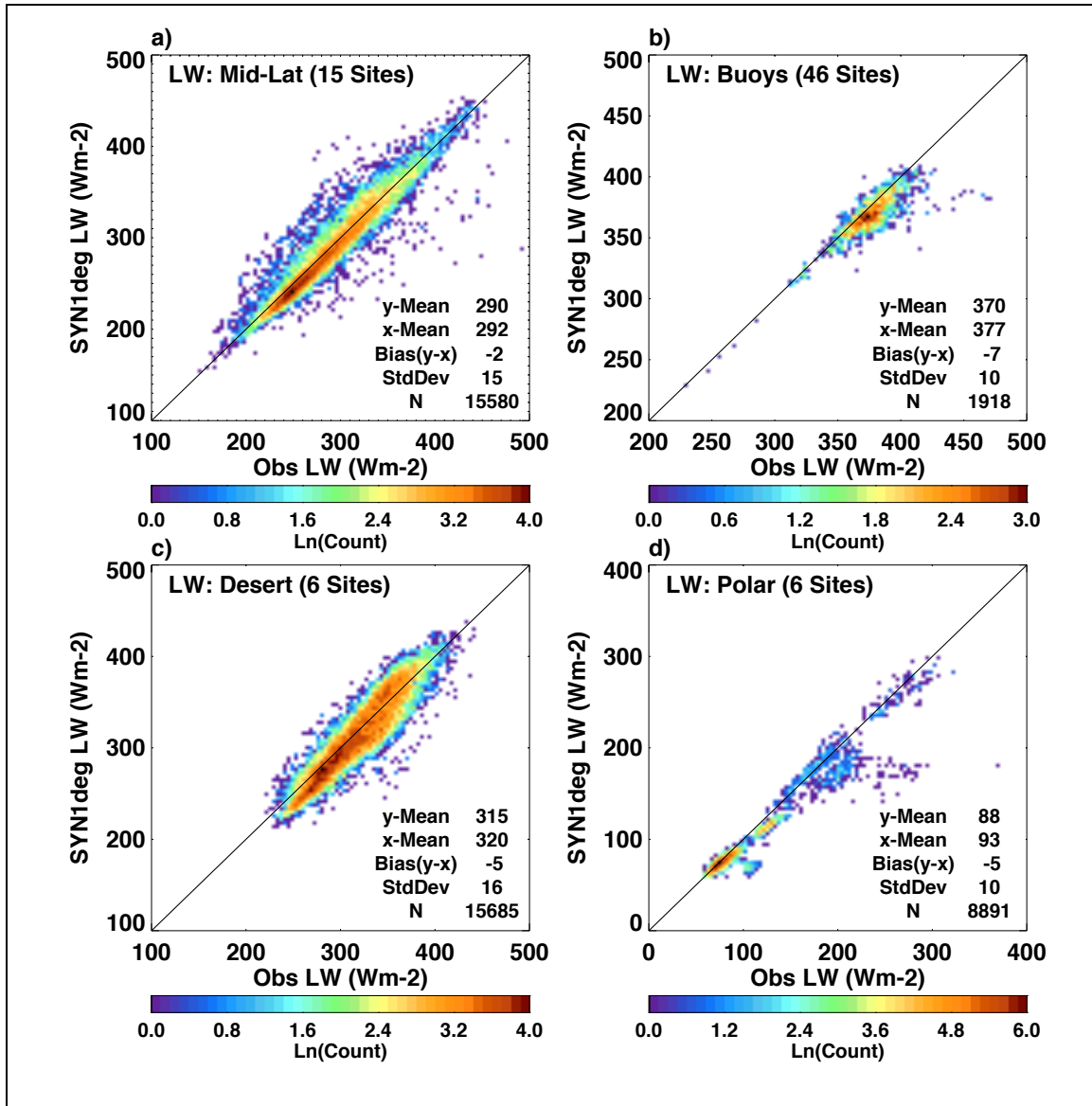
Figure 14. Comparisons of LW downward irradiance at the surface from the SYN1deg Ed4.1 calculations (y-axis for all plots) and BSRN and buoy surface sites (x-axis all plots). Data are from Mar 2000 through Feb 2020 and only include hours when a 1x1 grid box is 100% clear sky according to SYN1deg cloud fraction.

480

481 observations similar to those shown in **Fig. 13**. Except for the polar region, where DLI is

482 very sensitive to near surface air temperature, the bias and standard deviations of the DLI

483 is smaller than the SW equivalents in terms of both Wm^{-2} and percentage of the mean

484 observation. Depending on aerosol type, DLI is less sensitive to total AOD. For example,

485 a doubling of AOD (0.2 to 0.4) for a continental aerosol type results in a DLI change of

486 only 0.2 W m^{-2}. Table 6, however, shows the sensitivity of DLI (and DSI) to changes in

487 dust particle size and shows that for LW, a change in aerosol type results in up to a 10

488 Wm^{-2} change in DLI.

Table 6. Effect of Dust Particle size on Surface Irradiance Calculations[1]

	Dust Particle Size (microns)		
	0.5	2.0	8.0
DLI	352 Wm^{-2}	359 Wm^{-2} (+2.0%)	362 Wm^{-2} (+2.8%)
DSI	1046 Wm^{-2}	1038 Wm^{-2} (-0.7%)	1020 Wm^{-2} (-2.5%)
[1]The radiative transfer code is run for a Mid-Latitude Summer atmosphere, open shrub surface albedo, aerosol scale height of 1.5km, clear sky, and cosine solar zenith angle of 1.0. Aerosol optical depth is fixed at 0.2 for all calculations.			

489

490 DLI is thus more sensitive to aerosol type in certain regions of the globe where there is

491 substantial dust. To see the potential impact on DLI **Figure 15** shows calculated LW

492 downward radiative forcing (clear minus pristine calculations) at 57 AERONET sites

493 across the 20 years of SYN1deg data under consideration. The Northwest Africa sites

494 (where dust is found seasonally) are shown as red boxes where one clearly sees larger

495 LW forcing at these sites. Given the importance of particle size to LW effect we check

496 MATCH particle size against AERONET fine/coarse mode retrievals for several of the

497 African AERONET sites. **Figure 16** plots canonical mean observations of fine and coarse

498 mode AOD from three AERONET sites along with groupings of AOD species from the

499 MATCH model output. To compare to AERONET fine mode observations we plot the

500 sum of the MATCH AOD due to organic carbon (OC), black carbon (BC) and sulfate

501   (SO4). We compare the sum of MATCH AOD large dust particles (> 1 μm) along with

502   sea salt (though sea salt is essentially zero over land) to the coarse mode AERONET

503   optical depth. All AOD values are at 550nm.

504
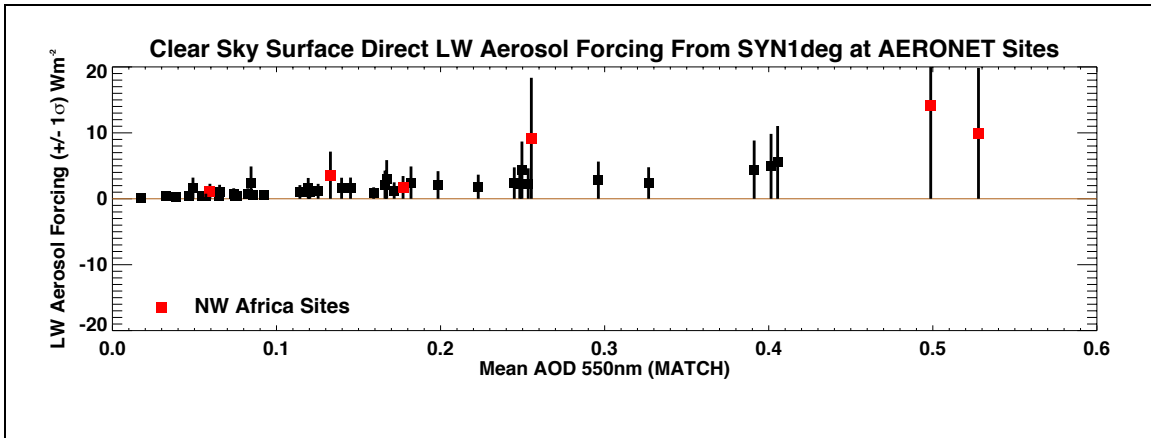
Figure 15. Clear sky direct radiative effect (clear minus pristine) in downward longwave irradiance averaged from 2000 through 2020 when AERONET observations are available. Boxes indicate average, vertical bar is +/- one standard deviation. Black boxes indicate all 57 AERONET sites and red boxes indicate Northwest Africa sites.

505

506   **Figure 16** indicates that resultant fine/coarse mode comparisons are encouraging but the

507   agreement is site dependent. In general MATCH is capturing seasonal changes in fine

508   and coarse particles at these sites but the magnitude of the AODs is biased.

509
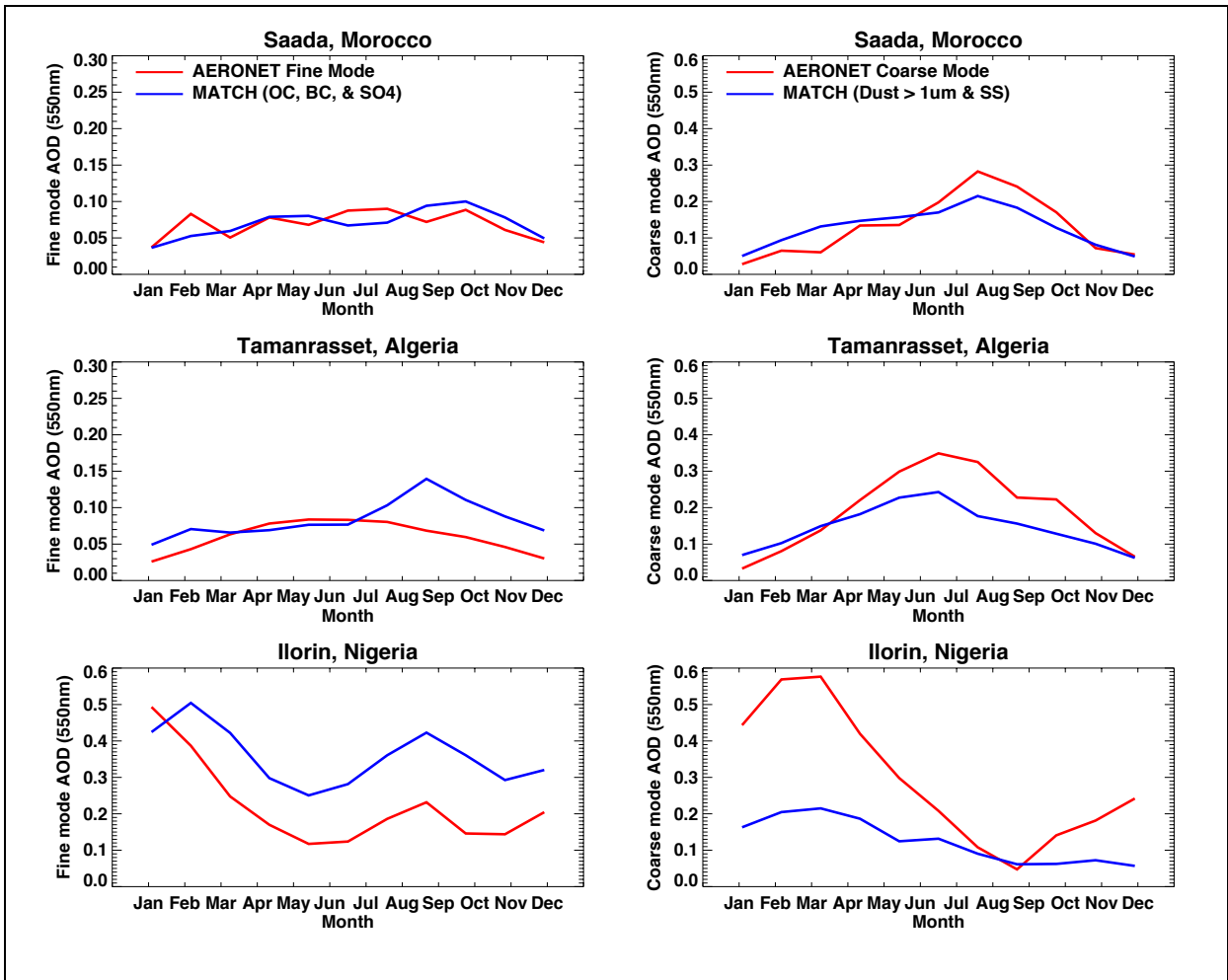
Figure 16. Canonical monthly means across 20 years (2000-2020) showing AERONET fine (left) and coarse (right) AOD at 550nm compared to MATCH constituents. MATCH values represent summations of organic, black carbon (OC, BC) and sulfate (SO4) for fine mode and large dust particles (> 1micron) plus sea salt for coarse mode comparisons.

510

511   **4.3 CERES TOA and EBAF-surface comparison**

512   CERES instruments observe TOA irradiances, which can be used to assess the

513   bias in computed irradiance. Global annual mean clear-sky TOA irradiances derived from

514   CERES observation averaged over 20 years from March 2000 through February 2020 are

515   53 Wm^{-2} for reflected shortwave irradiance and 268 Wm^{-2} for emitted longwave

516   irradiance. Corresponding computed reflected shortwave flux is 51 Wm^{-2} and emitted

517   longwave flux is 267 Wm^{-2}. Insight into the surface irradiance errors may be gained by

518   considering how surface irradiance is modified via the tuning algorithm to match TOA

519   irradiance in the CERES EBAF-surface product (Kato et al. 2018). After known biases

520   are taken out, the adjustment of temperature and specific humidity profiles, surface and

521   aerosol properties are derived based on their pre-assigned uncertainty and the difference

522   of computed and observed TOA shortwave and longwave irradiance using the Lagrange

523   multiplier approach. To match the computed shortwave and longwave fluxes, AOD is

524   increased from 0.136 to 0.156 (global annual mean values) and precipitable water is

525   decreased from 2.29 cm to 2.22 cm (global annual mean values). These adjustments

526   change the downward shortwave irradiance from 244 Wm^{-2} to 243 Wm^{-2}.

527   To analyze how the EBAF tuning process changes surface irradiance, AOD and

528   precipitable water, we computed the mean change separated by surface group shown in

529   **Fig 11**. Generally, AOD increases and precipitable water decreases to increase reflected

530   shortwave flux, which in turn decreases surface downward shortwave irradiance over

531   these regions (**Table 6**). For the midlatitude group, on average, AOD is increased by

532   0.02, precipitable water is decreased by 0.06 cm, and surface albedo is increased by 0.03.

533   These adjustments reduce the diurnally averaged downward shortwave irradiance at the

534   surface by 2 Wm^{-2}. We do not have exact matches of BSRN and AERONET surface sites

535   but Tables 3 and 4 show MATCH AODs have either no bias (north America and China

536   and southeast Asia) or slightly negatively biased by 0.01 (Europe). Therefore, increasing

537   MATCH AODs by 0.02 on average for the mid-latitude group seems justifiable.

538   However, decreasing 2 Wm^{-2} for the diurnally averaged downward shortwave is smaller

539   than the 11 Wm^{-2} bias shown in the top left plot of **Fig. 13**, although instantaneous

540   irradiances are used for **Fig. 13**. The positive bias found in the downward shortwave

541   irradiance for the North Africa group (**Fig 13c**) is not consistent with the positive bias of

542   aerosol optical depth shown in **Table 3** under clear-sky conditions.

543   The adjustment made to match TOA shortwave irradiance, in the EBAF product,

544   is within the uncertainty of MODIS-derived AOD of ±0.05 over land and ±0.03 over

545   ocean (Remer et al. 2008; Levy et al. 2010, 2013). However, these are an expected error

546   of instantaneous AOD retrieval derived from the comparison of AODs with AERONET.

547   Therefore, the bias averaged over ground sites and many years is expected to be much

548   smaller. Although, the 0.03 AOD adjustment over ocean might be the upper limit of the

549   uncertainty of MODIS AODs over ocean, 16 Wm^{-2} bias in the instantaneous downward

550   shortwave irradiance seems to be larger than the reduction by 2 Wm^{-2} in the diurnally

551   averaged downward shortwave irradiance.

552   While we cannot identify the cause of the discrepancy between AOD comparison

553   and downward shortwave irradiance comparison with surface observations, potential

554   issues are following. 1) Aerosol type and optical properties used in irradiance

555   computations, and 2) bias in downward shortwave irradiance measured by pyranometer,

556   especially diffuse irradiance at smaller solar zenith angles. Because of the temperature

557   gradient within pyranometer, the downward shortwave irradiance measured by a

558   pyranometer tends to be biased low under clear-sky condition (Haeffelin et al. 2001).

559   Note that a study by Ham et al. (2020) indicates that the bias of diurnally averaged

560   surface downward shortwave irradiance computed by a four-stream model should be

561   smaller than 1%.

562

563

Table 6: Radiative flux, aerosol optical depth (AOD), precipitable water, and surface albedo change to match observed top-of-atmosphere radiative fluxes

Site	Observed TOA upward shortwave irradiance (Wm-2)	Changes: Adjusted - Unadjusted				
		Clear-sky TOA upward shortwave irradiance (Wm-2)	Clear-sky surface downward shortwave irradiance (Wm-2)	Clear-sky AOD	Clear-sky precipitable water (cm)	Clear-sky surface albedo
Mid-Latitude	63.3	3.9	-2.0	0.02	-0.06	0.03
Desert	92.3	3.4	-1.7	0.02	-0.04	0.01
Polar	86.5	8.2	-0.2	0.01	-0.03	0.10
Buoys	42.0	1.6	-2.0	0.03	-0.12	0.00

564

565 **5. Conclusions**

566   We evaluated MATCH aerosol optical depth used to produce the CERES

567 SYN1deg product. Aerosol optical depths derived from Terra and Aqua by the dark target

568 and deep blue algorithms were merged to produce daily gridded AODs. Daily gridded

569 AODs were used for assimilation by MATCH at local solar noon. As a consequence,

570 monthly mean AODs under clear-sky conditions identified by MODIS closely agree with

571 those derived from MODIS, although MATCH uses climatological aerosol sources.

572 Because AODs are not screened by QAC, MATCH AODs are larger over convective

573 regions (e.g. Amazon, central Africa, and south east Asia) for both clear-sky and all-sky

574 conditions.

575   MATCH AODs under all-sky conditions are larger than those under clear-sky

576 conditions. Time series of AERONET AODs indicate that AODs generally increase with

577 cloud fraction, which is consistent with, primarily, water uptake by hygroscopic aerosols

578 (Varnai et al, 2017). In addition, surface observations at the ARM SGP site suggest that a

579 larger AODs and larger precipitable water under all-sky conditions than those under

580 clear-sky conditions. Aerosol optical depth biases from AERONET AODs are

581 comparable to biases of MERRA2 AOD biases from AERONET AODs for both all-sky

582 and clear-sky conditions. However, MERRA2, which uses AERONET AODs to train the

583 algorithm, has better temporal correlation with AERONET AODs than MATCH AODs.

584   Once MATCH AODs are used for surface irradiance computations, downward

585 shortwave irradiances are positively biased by 1% to 2% compared to those observed at

586 surface sites. Top-of-atmosphere reflected clear-sky shortwave irradiances are negatively

587 biased compared with those derived from CERES observations. Increasing AODs by

588 ~0.02, and surface albedos by 0.03, and decreasing precipitable water by 0.06 cm over

589 mid-latitude surface sites makes computed reflected TOA irradiances agree with those

590 derived from CERES. These adjustments reduce downward shortwave irradiances at the

591 surface by 2 Wm^{-2}. Decreasing MATCH AODs for the desert group is needed to match

592 computed reflected shortwave irradiances at TOA with those derived from CERES.

593 However, decreasing MATCH AODs is not consistent with generally larger MATCH

594 AODs compared with AERONET.

595   Optical properties of aerosols (i.e. aerosol type) play a role in computing

596 shortwave and longwave irradiance and changing and/or incorrect aerosol type can alter

597 the downward irradiances. Aerosol types used in the computations rely on the mapping of

598 MATCH types to those available in the radiative transfer model (Table 2). Biases in the

599 fraction of each aerosol type and their optical properties can change TOA upward and

600 surface downward shortwave irradiances without altering total AOD. A fuller evaluation

601 of aerosol type is left for future study.

602

603 **Acknowledgments**

604   This work was funded by the NASA CERES project. The products and the

605 validation could not have been accomplished without the help of the CERES TISA team.

606 These data were obtained from the NASA Langley Research Center EOSDIS Distributed

607 Active Archive Center. We also wish to acknowledge the hard work put in by the many

608 dedicated scientists maintaining surface instrumentation in many diverse climates to

609 obtain high quality observations of downwelling shortwave and longwave surface flux.

610 Those groups are noted in Appendix A. We would also like to thank the anonymous

611 reviewers for their in-depth reading and assessment of the paper which led to significant

612 improvements in the manuscript.

613

614

615

616

617

618

619

620

621

622

623

624

625

627

Appendix A. Surface Observation Sites Used for Validation

629   A great deal of data used in this study was collected by dedicated site scientists

630 measuring critical climate variables around the world. The tables included in this

631 appendix outline the sites, in situ measurements taken and their locations and dates of

632 available data. Table A1 lists the locations of the AERONET sites, our source for

633 observed aerosol optical depth which can be found on-line at:

634 https://aeronet.gsfc.nasa.gov/new_web/index.html.

635

Table A1. AERONET Observation Sites			
Region	Site	Location	Available Months
North Africa (5 Sites)	Saada, Morocco	31.6N, 8.2W	2004/07 - 2019/04
	Ouarzazate, Morocco	30.9N, 6.9W	2012/02 - 2015/06
	Dhaka, Morocco	23.7N, 15.9W	2002/02 - 2005/11
	Tamanrasset, Algeria	22.8N, 8.2E	2004/07 - 2019/04
	Cape Verde Island	16.7N, 22.9W	2000/03 - 2018/12
Central Africa (5 Sites)	Ilorin, Nigeria	8.5N, 4.7E	2000/03 - 2019/09
	Koforidua, Ghana	6.1N, 0.3W	2012/12 - 2019/04
	Lope, Gabon	0.2S, 11.6E	2014/04 - 2018/02
	Mbita, Kenya	0.4S, 34.2E	2006/03 - 2017/17
	Bujumbura, Burundi	3.4S, 29.4E	2013/12 - 2019/04
China, Korea (8 Sites)	Xinglong, China	40.4N, 117.6E	2006/02 - 2014/11
	Beijing, China	39.9N, 116.4E	2001/03 - 2019/03
	Anymon Isl, S Korea	36.5N, 126.3E	2000/03 - 2019/11
	Yonsei Univ, S Korea	37.6N, 126.9E	2011/03 - 2019/01
	Cuiying Mt, China	35.9N, 104.1E	2006/07 - 2013/05
	Nanjing, China	32.2N, 118.7E	2008/03 - 2010/04
	Taihu, China	31.4N, 120.2E	2005/09 - 2016/08
	XiangHe, China	39.7N, 116.9E	2001/03 - 2017/05
India, SE Asia (8 Sites)	Gandhi College, India	25.8N, 84.1E	2006/04 - 2019/11
	Luang Namtha, Laos	20.9N, 101.4E	2001/04 - 2019/02
	Omkoi, Thailand	17.8N, 98.4E	2003/02 - 2018/03
	Dhaka Univ, Bangledesh	23.7N, 90.3E	2012/06 - 2019/07
	Bhola, Bangledesh	22.2N, 90.7E	2013/04 - 2019/04
	Nghia Do, Vietnam	21.0N, 105.8E	2010/11 - 2019/09
	Pune, India	18.5N, 73.8E	2004/10 - 2019/06
	Hanimaadhoo, Maldives	6.7N, 73.2E	2004/11 - 2019/09

636

637

638

639

640

641

Table A1. AERONET Observation Sites (Continued)			
Region	Site	Location	Available Months
Brazil (7 Sites)	Petrolina, Brazil	9.1S, 40.4W	2004/07 - 2016/11
	Abracos Hill, Brazil	10.7S, 62.4W	2000/03 - 2005/10
	Alta Floresta, Brazil	9.9S, 56.1W	2000/05 - 2019/02
	Belterra, Brazil	2.6S, 55.0W	2000/03 - 2005/04
	Ji Parana SE, Brazil	10.9S, 61.9W	2006/01 - 2017/10
	Manaus, Brazil	2.9S, 60.0W	2011/02 - 2019/05
	Rio Branco, Brazil	9.9S, 67.9W	2000/07 - 2017/10
Australia (6 Sites)	Jabiru, Australia	12.6S, 132.9E	2000/03 - 2019/09
	Lake Argyle, Australia	16.1S, 128.7E	2001/10 - 2019/09
	Canberra, Australia	35.3S, 149.1E	2003/01 - 2017/08
	Birdsville, Australia	25.9S, 139.3E	2005/08 - 2018/06
	Lucinda, Australia	18.5S, 146.4E	2009/10 - 2020/01
	Lake Lefroy, Australia	31.2S, 121.7E	2012/06 - 2019/12
North America (10 Sites)	Brats Lake, Canada	50.2N, 104.7W	2000/03 - 2013/02
	Sioux Falls, SD	43.7N, 96.6W	2001/06 - 2017/10
	Ames, IA	42.0N, 93.8W	2004/05 - 2019/03
	Boulder Tower	40.0N, 105W	2001/05 - 2016/07
	Bondville, IL	40.0N, 88.4W	2000/03 - 2017/10
	Brookhaven, NY.	40.8N, 72.9W	2002/09 - 2020/01
	Wallops Island, VA	37.9N, 75.5W	2003/03 - 2020/03
	ARM/SGP E13	36.6N, 97.5W	2000/03 - 2018/05
	Chesapeake Light Tower	36.9N, 75.7W	2000/03 - 2016/01
	Table Mountain, CO	40.1N, 105.2W	2008/11 - 2017/12
Europe (10 Sites)	Cabauw, Netherlands	51.9N, 4.9E	2003/04 - 2017/11
	Palaiseau, France	48.7N, 2.2E	2000/03 - 2020/10
	Torevere, Estonia	58.2N, 26.5E	2002/06 - 2019/07
	Kishinev, Moldova	47.0N, 28.8E	2000/03 - 2018/11
	Belsk, Poland	51.8N, 20.8E	2004/01 - 2016/08
	Kyiv, Ukraine	50.3N, 30.5E	2007/04 - 2018/12
	Hamburg, Germany	53.5N, 9.9E	2000/06 - 2018/06
	Munich Univ, Germany	48.1N, 11.6E	2001/11 - 2019/05
	Thessaloniki, Greece	40.6N, 22.1E	2003/06 - 2020/03
	Bucharest, Hungary	44.3N, 26.0E	2000/10 - 2019/03

642

643   Sources of surface observed downwelling irradiance are outlined in Tables

644   A2 (land) and A3 (buoys). For land we utilize data from the Baseline Surface

645   Radiation Network (BSRN) (Dreimel et al, 2018; Ohmura et al. (1998)), the US Dept.

646   of Energy's Atmospheric Radiation Measurement (ARM) program and NOAA's

647   SURFRAD network available from NOAA's Air Resources Laboratory/Surface

648   Radiation Research Branch., Augustine et al. (2000). Buoy observations come from

649   two sources through four separate projects. The Upper Ocean Processes group at

650   Woods Hole Oceanographic Institute have maintained the Stratus, North Tropical

651   Atlantic Site (NTAS) and Hawaii Ocean Time Series (HOTS) buoys for more than a

652   decade providing valuable time series of radiation observations in climatically

653   important regions of the ocean. These data can be retrieved from:

654   http://uop.whoi.edu/index.html. We would also like to acknowledge the Project

655   Office of NOAA's Pacific Marine Environmental Labs (PMEL) where three groups of

656   buoy data were downloaded: In the Pacific, the Tropical Atmosphere

657   Ocean/Triangle Trans-Ocean Buoy Network (TAO/TRITON) (McPhaden, 2002) data,

658   from the tropical Atlantic Ocean, the Prediction and Research Moored Array in the

659   Tropical Atlantic (PIRATA) (Servain et al. 1998), and the Research Moored Array for

660   African - Asian - Australian Monsoon Analysis and Prediction (RAMA) (McPhaden et

661   al., 2009) in the Indian Ocean. Also downloaded from PMEL are the long-term buoy

662   observations PAPA and Kuroshio Current observatory sites.

663

664

665

666

667

668

669

670

671

672

673

Table A2. Surface Irradiance Validation Sites (Land)

Region	Site	Location	Source
Mid-Latitude (15 Sites)	Lindenberg, Germany	52.2N, 14.1E	BSRN
	Cabauw, Netherlands	51.9N, 4.9E	BSRN
	Fort Peck, MT	48.3N, 105.1W	BSRN
	Payerne, Switzerland	46.8N, 6.9E	BSRN
	Penn State, PA	40.7N, 77.9W	SURFRAD
	Beijing, China	39.9N, 116.3E	BSRN
	E13, Lamont, OK	36.6N, 97.5W	ARM
	Ches Light Tower, USA	36.9N, 75.7W	BSRN
	Tateno, Japan	36.1N, 140.1E	BSRN
	Goodwin Creek, MS	34.2N, 89.9W	SURFRAD
	De Aar, South Africa	30.6S, 24.0E	BSRN
	Lauder, New Zealand	45.0S, 169.7E	BSRN
	Florianapolis, Brazil	27.5S, 48.5W	BSRN
	Brasilia, Brazil	15.6S, 47.7W	BSRN
	Sao Martinho da Serra, Brazil	29.4S, 53.8W	BSRN
Desert (6 Sites)	Sede Boqer, Israel	30.8N, 34.7E	BSRN
	Saudi Solar Village	24.9N, 46.4E	BSRN
	Tamanrasset, Algeria	22.8N, 5.5E	BSRN
	Desert Rock, NV	36.6N, 116.1W	SURFRAD
	Alice Springs, Australia	23.7S, 133.8E	BSRN
	Gobabeb, Namibia	23.5S, 15.0E	BSRN
Polar (6 Sites)	Alert,Canada	82.5N, 62.4W	BSRN
	Tiksi, Russia	71.6N, 128.9E	BSRN
	Barrow, Alaska	71.3N, 156.7W	BSRN
	Syowa, Antarctica	69.0S, 39.5E	BSRN
	South Pole, Antarctica	90.0S, 0.5E	BSRN
	G. von Neumayer, Antarctica	-70.6S, 8.3W	BSRN

674 BSRN: Baseline Surface Radiation Network, http://bsrn.awi.de/
675 SURFRAD: NOAA- SURFace RADiation Program, http://www.esrl.noaa.gov/gmd/grad/surfrad/
676 ARM: US Dept of Energy, Atmospheric Radiation Measurement Program, http://www.arm.gov/

677

Table A3. Surface Observation Sites for Ocean Buoy Locations

Program Name	Data Source	Locations
Upper Ocean Processes Group (UOP) 3 Buoys	Woods Hole Oceanographic Institute	Stratus Buoy -20.2N, 85.0W
		North Tropical Atlantic Buoy 14.5N, 51.0W
		Hawaii Ocean Time Series Buoy 22.5N, 158W
PIRATA Buoys 14 Buoys	Pacific Marine Environmental Laboratory (PMEL)	East Atlantic Ocean
RAMA Buoys 10 Buoys	PMEL	Tropical Indian Ocean
TAO Array Buoys 17 Buoys	PMEL	E & W Tropical Pacific Ocean
Kuroshio Extension Observatory Buoy	PMEL	NW Pacific, 32.4N, 144.6E
PAPA Sub-Arctic Ocean Buoy	PMEL	NE Pacific, 50.1N, 144.8W

678 UOP: http://uop.whoi.edu/projects/projects.htm
679 PMEL: http://www.pmel.noaa.gov/tao/data_deliv/deliv.html

680

681

References

Augustine, J. A., DeLuisi, J. J., and Long, C. N.: SURFRAD – A national surface radiation
budget network for atmospheric research, Bull. of Amer. Met. Soc. 81, No. 10, pp.
2341-2358, 2000.

Barth, M. C., Rasch, P. J., Kiehl, J. T., Benkovitz, C. M., and Schwartz, S. E.: Sulfur
chemistry in the NCAR CCM: Description, evaluation, features and sensitivity to
aqueous chemistry, J. Geophys. Res., 106, 20 311–20 322, 2000.

Bauer, S. E. and Menon, S.: Aerosol direct, indirect, semidirect, and surface albedo
effects from sector contributions based on the IPCC AR5 emissions for
preindustrial and present-day conditions, J. Geophys. Res., 117, D01206,
doi:10.1029/2011JD016816, 2012.

Benkovitz, C. M., Scholtz, M. T., Pacyna, J., Tarrason, L., Dignon, J., Voldner, E. C., Spiro,
P. A., Logan, J. A., and Graedel, T. E.: Global gridded inventories of anthropogenic
emissions of sulfur and nitrogen, J. Geophys. Res.: Atmos. 101 (D22), 29,239–
29,253, 1996.

Blanchard, D. C. and Woodcock, A. H.: The production, concentration and vertical
distribution of the sea-salt aerosol, Ann. Of the NY Acad. Of Sci.,
doi:10.1111/j.1749-6632.1980.tb17130, 1980.

Boucher, O., Randall, D., Artaxo, P., Bretherton, C., Feingold, G., Forster, P., Kerminen,
V.-M., Kondo, Y., Liao, H., Lohmann, U., Rasch, P., Satheesh, S.K., Sherwood, S.,
Stevens, B. and Zhang, X. Y.: Clouds and Aerosols. In: Climate Change 2013: The

703   Physical Science Basis. Contribution of Working Group I to the Fifth Assessment

704   Report of the Intergovernmental Panel on Climate Change [Stocker, T.F., D. Qin,

705   G.-K. Plattner, M. Tignor, S.K. Allen, J. Boschung, A. Nauels, Y. Xia, V. Bex and P.M.

706   Midgley (eds.)]. Chapter 7. Cambridge University Press, Cambridge, United

707   Kingdom and New York, NY, U, 2013.

708   Colbo, K. and Weller, R. A.: Accuracy of the IMET sensor package in the subtropics. J.

709   Atmos. Oceanic Technol., 26, 1867–1890,

710   https://doi.org/10.1175/2009JTECHO667.1, 2009.

711   Collins, W. D., Rasch, P. J., Eaton, B. E., B. Khattatov, V., Lamarque, J-F. and Zender, C.

712   S.: Simulating aerosols using a chemical transport model with assimilation of

713   satellite aerosol retrievals: Methodology for INDOEX. J. Geophys. Res., 106 (D7),

714   7313–7336, 2001.

715   d' Almeida, G. A., P. Koepke and E. P. Shettle: Atmospheric Aerosols: Global

716   Climatology and Radiative Characteristics. A. Deepak Publishing, 561 pp. 1991

717   Driemel, A., and Co-authors: Baseline Surface Radiation Network (BSRN): structure and

718   data description (1992–2017), Earth Syst. Sci. Data, 10, 1491-1501,

719   doi:10.5194/essd-10-1491-2018. 2018

720   Emmons, L. K., and co-authors: Description and evaluation of the Model for Ozone and

721   Related chemical Tracers, version 4 (MOZART-4), Geosci. Model Dev., **3**, 43–67.

722   www.geosci-model-dev.net/3/43/2010/, 2010.

723   Fu, Q. and Liou, K-N.: Parameterization of the radiative properties of cirrus clouds, J.

724   Atmos. Sci., 50, 2008–2025, 1993.

725   Fu, Q., Lesins, G., Higgins, J., Charlock, T., Chylek, P. and Michalsky, J.: Broadband

726   water vapor absorption of solar radiation tested using ARM data. Geophys. Res. Let.,

727   25, 1169–1172, 1998.

728   Ginoux, P., Chin, M., Tegen, I., Prospero, J. M., Holben, B., Dubovik, O. and Lin, S-J.:

729   Sources and distributions of dust aerosols simulated with the GOCART model J. of

730   Geophys. Res.: Atmos., 106, 20255-20273, doi.org/10.1029/2000JD000053, 2001.

731   Haeffelin, M., Kato, S., Smith, A. M., Rutledge, C. K., Charlock T. P. and Mahan, J. R.:

732   Determination of the thermal offset of the Eppley precision spectral pyranometer,

733   Appl. Opt. 40, 472-484, 2001.

734   Ham, S., Kato, S. and Rose, F. G.: Examining biases in diurnally-integrated shortwave

735   irradiances due to two- and four-stream approximations in cloudy atmosphere. J.

736   Atmos. Sci., 77(2), 551–581. doi: 10.1175/JAS-D-19-0215.1, 2020.

737   Hess, M., Koepke, P. and Schult, I.: Optical Properties of Aerosols and Clouds: The

738   software package OPAC. Bull. Amer. Meteor. Soc., 79, 831-844.

739   https://doi.org/10.1175/1520-0477(1998)079<0831:OPOAAC>2.0.CO;2,1998.

740   Holben B.N., Eck, T. F., Slutsker, I., Tanre, D., Buis, J. P., Setzer, A., Vermote, E.,

741   Reagan, J. A., Kaufman, Y., Nakajima, T., Lavenu, F., Jankowiak, I. and Smirnov,

742   A.: AERONET - A federated instrument network and data archive for aerosol

743   characterization, Rem. Sens. Environ., 66, 1-16, 1998

744   Hsu, N. C., Tsay, S-C, King, M. D. and Herman, J. R.: Deep Blue Retrievals of Asian

745   Aerosol Properties During ACE-Asia, IEEE Trans. On Geosci. and Rem. Sens.,

746   44(11), 2006.

747 Huneeus, N., and co-authors: Global dust model intercomparison in AeroCom phase I,

748 Atmos. Chem. Phys., 11, 7781–7816. www.atmos-chem-phys.net/11/7781/2011/

749 doi:10.5194/acp-11-7781-2011, 2011.

750 Kato, S., Loeb, N. G., Rose, F. G., Doelling, D. R., Rutan, D. A., Caldwell, T. E., Yu L.

751 and Weller, R. A.: Surface irradiances consistent with CERES-derived top-of-

752 atmosphere shortwave and longwave irradiances. J. of Clim Dyn. doi: 10.1175/JCLI-

753 D-12-00436, 2013.

754 Kato, S., Rose, F. G., Rutan, D. A., Thorsen, T. J., Loeb, N. G., Doelling, D. R., Huang,

755 X., Smith, W. L., Su, W. and Ham, S-H.: Surface Irradiances of Edition 4.0 Clouds

756 and the Earth's Radiant Energy System (CERES) Energy Balanced and Filled

757 (EBAF) Data Product. J. of Clim Dyn. doi: 10.1175/JCLI-D-17-0523.1, 2018.

758 Kaufman, Y. and co-authors: A critical examination of the residual cloud contamination

759 and diurnal sampling effects on MODIS estimates of aerosol over ocean, IEEE Trans.

760 Geosci. Rem. Sens. 43, DOI: 10.1109/TGRS.2005.858430, 2005.

761 Kinne, S. and co-authors: An AeroCom initial assessment – optical properties in aerosol

762 component modules of global models. Atmos. Chem. Phys., 6, 1815–1834.

763 www.atmos-chem-phys.net/6/1815/2006/, 2006.

764 Koch, D., and co-authors: Evaluation of black carbon estimations in global aerosol

765 models. Atmos. Chem. Phys., 9, 9001–9026. www.atmos-chem-

766 phys.net/9/9001/2009/, 2009.

767 L'Ecuyer T. S., Beaudoing, H. K., Rodell, M., Olson, W., Lin, B., Kato, S., Clayson, C.

768 A., Wood, E., Sheffield, J., Adler, R., Huffman, G., Bosilovich, M., Gu, G.,

769 Robertson, F., Houser, P. R., Chambers, D., Famiglietti, J. S., Fetzer, E., Liu, W. T.,

770   Gao, X., Schlosser, C. A., Clark, E., Lettenmaier, D. P. and Hilburn, K.: The

771   observed state of the energy budget in the early twenty-first century. J Clim

772   28(21):8319–8346. https://doi.org/10.1175/Jcli-D-14-00556.1, 2015.

773 Levy, R. C., Remer, L. A., Kleidman, R. G. , Mattoo, S., Ichoku, C., Kahn R. and Eck, T.

774   F.: Global evaluation of the collection 5 MODIS dark-target aerosol products over

775   land. Atmos. Chem and Phys., 10, 103999-10420. https://doi.org/10.5194/acp-10-

776   10399-2010, 2010.

777 Levy, R. C., Mattoo, S., Munchak, L. A., Remer, L. A., Sayer, A. M., Patadia, F. and

778   Hsu, N. C.: The Collection 6 MODIS aerosol products over land and ocean. Atmos.

779   Meas. Tech., 6, 2989-3034, 10.5194/amt-6-2989-2013, 2013.

780 Liousse, C., Penner, J. E., Chuang, C., Walton, J. J., Eddleman, H. and Cachier, H.: A

781   global three-dimensional model study of carbonaceous aerosols, J. Geophys. Res. A.,

782   101(D14), 19 411– 19 432, 1996.

783 Loeb, N. G., Kato, S., Loukachine, K. and Smith, N. M.: Angular Distribution Models for

784   Top-of-Atmosphere Radiative Flux Estimation from the Clouds and the Earth's

785   Radiant Energy System Instrument on the Terra Satellite. Part I: Methodology, J.

786   Atmos. Oceanic Technol, 22, 338-351, 2005.

787 Loeb, N. G. and Su, W.: Direct Aerosol Radiative Forcing Uncertainty Based on a

788   Radiative   Perturbation   Analysis.   J.   Climate,   23(19),   5288-5293.   doi:

789   10.1175/2010JCLI3543.1, 2010.

790 Loeb, N. G., Doelling, D. R., Wang, H., Su, W., Nguyen, C., Corbett, J. G., Liang, L., Mitrescu,

791   C., Rose, F. G. and Kato, S.: Clouds and the Earth's Radiant Energy System (CERES)

792   Energy Balanced and Filled (EBAF) top-of-atmosphere (TOA) Edition-4.0 data

793   product. J. Climate, 31, 895–918, https://doi.org/10.1175/JCLI-D-17-0208.1,

794   2018.

795   Loeb, N. G., Rose, F. G., Kato, S., Rutan, D. A., Su, W., Wang, H., Doelling, D. R., Smith, W.

796   L. and Gettelman, A.: Toward a Consistent Definition between Satellite and Model

797   Clear-Sky Radiative Fluxes, J. Clim. DOI: 10.1175/JCLI-D-19-0381.1, 2020.

798   Long, C. N., Ackerman, T. P., Gaustad, K. L. and Cole, J. N. S.: Estimation of fractional

799   sky cover from broadband shortwave radiometer measurements, J. Geophys.

800   Res.,111, D11204, doi:10.1029/2005JD006475, 2006.

801   Martins, J. V., D. Tanre, D., Remer, L., Kaufman, Y., Mattoo, S. and Levy, R.: MODIS cloud

802   screening for remote sensing of aerosols over oceans using spatial variability,

803   Geophys. Res. Lett., 29, 1619, DOI:10.1029/2001GL013252, 2002.

804   Marshak, A., Ackerman, A., da Silva, A. M., Eck, T., Holben, B., Kahn, R., Kleidman, R.,

805   Knobelspiesse, K., Levy, R., Lyapustin, A., Oreopoulos, L, Remer, L., Torres, O.,

806   Várnai, T., Wen, G., and Yorks, J.: Aerosol properties in cloudy environments from

807   remote sensing observations, Bul. Amer. Met. Soc., 102, E2177–E2197,

808   https://doi.org/10.1175/BAMS-D-20-0225.1, 2021.

809   McPhaden, M. J.: TAO/TRITON tracks Pacific Ocean warming in early 2002. CLIVAR

810   Exchanges, No. 24, International CLIVAR Project Office, Southampton, United

811   Kingdom, 7–9, 2002.

812   #——, and Coauthors: RAMA: The Research Moored Array for African–Asian–

813   Australian Monsoon Analysis and Pre- diction. Bull. Amer. Meteor. Soc., 90, 459–

814   480, doi:10.1175/ 2008BAMS2608.1, 2009.

815   Michalsky, J. J., Gueymard, C., Kiedron, P., McArthur, L. J. B., Philipona, R. and

816   Stoffel, T.: A proposed working standard for the measurement of diffuse horizontal

817   shortwave irradiance. J. of Geophys. Res. A., 112(D16),

818   https://doi.org/10.1029/2007JD008651, 2007.

819
820   Minnis, P., Sun-Mack, S., Chen, Y., Chang, F., Yost, C. R., Smith, W. L., Heck, P. W.,

821   Arduini, R. F., Bedka, S. T., Yi, Y., Hong, G., Jin, Z., Painemal, D., Palikonda, R.,

822   Scarino, B. R., Spangenberg, D. A., Smith, R. A., Trepte, Q. Z., Yang, P. and Xie, Y.:

823   CERES MODIS Cloud Product Retrievals for Edition 4–Part I: Algorithm Changes.

824   IEEE Transactions on Geoscience and Remote Sensing, 1-37. doi:

825   10.1109/TGRS.2020.3008866, 2020.

826   Ohmura A., Dutton, E., Forgan, B., Frohlich, C., Gilgen, H., Hegne, H., Heimo, A., Konig-

827   Langlo, G., McArthur, B., Muller, G., Philipona, R., Whitlock, C., Dehne, K. and Wild,

828   M.: Baseline Surface Radiation Network (BSRN/WCRP): New precision

829   radiometry for climate change research. Bull. Amer. Meteor. Soc., 79, No. 10,

830   2115-2136, 1998.

831   Randles, C. A., Da Silva, A. M., Buchard, V., Colarco, P. R., Darmenov, A., Govindaraju,

832   R., Smirnov, A., Holben, A., Ferrare, R., Hair, J., Shinozuka, Y. and Flynn, C. J.: The

833   MERRA-2 aerosol reanalysis, 1980 onward. Part I: System description and data

834   assimilation evaluation, J. Clim. 30(17), http://dx.doi.org/10.1175/ JCLI-D-16-

835   0609.s1, 2017.

836   Rasch, P. J., Mahowald, N. M. and Eaton, B. E.: Representations of transport,

837   convection, and the hydrologic cycle in chemical transport models: Implications

838   for the modeling of short-lived and soluble species. J. of Geo. Res., 102, 127-138,

839   1997.

840   Rasch, P. J., Collins, W. D. and Eaton, B. E.: Understanding the Indian Ocean

841   Experiment (INDOEX) aerosol distributions with an aerosol assimilation. J. of

842   Geo. Res., 106, 7337-7355, 2001.

843   Remer, L. A., and Co-authors: The MODIS aerosol algorithm, products, and validation. J.

844   Atmos. Sci., 62, 947–973, 2005.

845   Remer, L. A., Kleidman, R. G., Levy, R. C., Kaufman, Y. J., Tanre, D., Mattoo, S.,

846   Vanderlei Martins, J., Ichoku, C., Koren, I., Yu, H. and Holben, B. N.: Global aerosol

847   climatology from the MODIS satellite sensors. J. Geophys. Res.: A. 113(D14),

848   https://doi.org/10.1029/2007JD009661, 2008.

849   Rose, F. G, Rutan, D. A., Charlock, T., Smith, G. L. and Kato, S.: An Algorithm for the

850   Constraining of Radiative Transfer Calculations to CERES-Observed Broadband

851   Top-of-Atmosphere Irradiance. J. Atmos. and Ocean. Tech. 30, 1091-1106. DOI:

852   10.1175/JTECH-D-12-00058.1, 2013.

853   Rutan, D., Rose, F., Roman, M., Manalo-Smith, N., Schaaf, C. and Charlock, T.:

854   Development and assessment of broadband surface albedo from Clouds and the

855   Earth's Radiant Energy System clouds and radiation swath data product. J. Geophys.

856   Res., 114, D08125. doi:10.1029/2008JD010669, 2009.

857   Rutan, D., Kato, S., Doelling, D. R., Rose, F. G., Nguyen, L. T. and Caldwell, T.: CERES

858   Synoptic Product: Methodology and Validation of Surface Radiant Flux. J. Atmos.

859   And Ocean. Tech., 32, doi:10.1175/JTECH-D-14-00165.1, 2015.

860   Servain, J., Busalacchi, A. J., McPhaden, M. J., Moura, A. D., Reverdin, G., Vianna, M.

861   and Zebiak, S. E.: A Pilot Research Moored Array in the Tropical Atlantic

862   (PIRATA). Bull. Amer. Meteor. Soc., 79, 2019–2031, doi:10.1175/ 1520-

863   0477(1998)079,2019:APRMAI.2.0.CO;2. 1998

864   Sinyuk, A., Torres, O. and Dubovik, O.: Combined use of satellite and surface

865   observations to infer the imaginary part of refractive index of Saharan dust.

866   Geophysical Research Letters, 30(2), 1081. https://doi.org/10.1029/2002GL016189,

867   2003.

868   Smirnov, A., Holben, B. N., Eck, T. F., Dubovik, O. and Slutsker, I.: Cloud-screening

869   and quality control algorithms for the AERONET database. Rem. Sens. Env. 73, 337-

870   349, 2000.

871   Soden, B. and Chung, E-S.: The Large-Scale Dynamical Response of Clouds to Aerosol

872   Forcing. J. of Climate, 30, 8783-8794. doi: https://doi.org/10.1175/JCLI-D-17-

873   0050.1, 2017.

874   Stephens, G. L., Slingo, J. M., Rignot, E., Reager, J. T., Hakuba, M. Z., Durack, P. J.,

875   Worden, J. and Rocca, R.: Earth's water reservoirs in a changing climate. Proc. R.

876   Soc. A 476: 20190458. http://dx.doi.org/10.1098/rspa.2019.0458, 2020.

877   Su, W., Schuster, G. L., Loeb, N. G., Rogers, R. R., Ferrare, R. A., Hostetler, C. A., Hair,

878   J. W., and Obland, M. D.: Aerosol and cloud interaction observed from high spectral

879   resolution lidar data. J. of Geophys. Res.: Atmos., 113(D24), D24202.

880   Doi:10.1029/2008JD010588, 2008.

881   Su, W., Corbett, J., Eitzen, Z. and Liang, L.: Next-generation angular distribution models

882   for top-of-atmosphere radiative flux calculation from CERES instruments:

883   methodology. Atmos. Meas. Tech., 8(2), 611-632. doi: 10.5194/amt-8-611-2015,

884   2015.

885   Su, W., Corbett, J., Eitzen, Z. and Liang, L.: Next-generation angular distribution models

886   for top-of-atmosphere radiative flux calculation from CERES instruments: validation.

887   Atmos. Meas. Tech., 8(8), 3297-3313. doi: 10.5194/amt-8-3297-2015, 2015.

888   Su, W., G. L. Schuster, N. G. Loeb, R. R. Rogers, R. A. Ferrare, C. A. Hostetler, J. W.

889   Hair, M. D. Obland, 2008: Aerosol and cloud interaction observed from high spectral

890   resolution lidar data. J. of Geophy. Res,: Atmos., 113(D24), D24202.

891   Doi:10.1029/2008JD010588.

892   Textor, C. and Co-authors: Analysis and quantification of the diversities of aerosol

893   life cycles within AeroCom, Atmos. Chem. Phys., 6, 1777-1813. www.atmos-

894   chem-phys.net/6/1777/2006/, 2006.

895   Textor, C., and Co-authors: The effect of harmonized emissions on aerosol

896   properties in global models – an AeroCom experiment. Atmos. Chem. Phys., 7,

897   4489–4501. www.atmos-chem-phys.net/7/4489/2007/, 2007.

898   Varnai, T., Marshak, A. and Eck, T. F.: Observation-based study on aerosol optical depth

899   and particle size in partly cloudy regions. J. Geophys. Res: A. 122, 10,013–10,024,

900   https://doi.org/10.1002/2017JD027028, 2017.

901   Wen, G., Marshak, A., Cahalan, R. F., Remer, L. A. and Kleidman, R. G.: 3-D aerosol-

902   cloud radiative interaction observed in collocated MODIS and ASTER images of

903   cumulus cloud fields, J. Geophys. Res., 112, D13204, doi:10.1029/2006JD008267,

904   2007.

905   Wielicki, B. A., Barkstrom, B. R., Harrison, E. F., Lee, R. B. III, Smith, G. L. and Cooper, J.

906   E.: Clouds and the Earth's Radiant Energy System (CERES): An Earth Observing

907   System Experiment. Bull. Amer. Meteor. Soc., 77, 853-868, 1996.

908   Zender, C. S., Huishen, B. and Newman, D.: Mineral Dust Entrainment and Deposition

909   (DEAD) model: Description and 1990s dust climatology. J. Geophys. Res., 108,

910   doi:10.1029/2002JD002775, 2003.